Geostratigraphic mapping of the intrusive Valentine Domes on the Moon

Javier Eduardo Suárez-Valencia[1], Angelo Pio Rossi[1]

[1]Constructor University, Bremen, Germany.

Corresponding author: Javier Eduardo Suarez-Valencia (jsuarezvalencia@constructor.university)

This manuscript is a non-peer reviewed preprint of an article submitted to the Journal of Geophysical Research: Planets.

Abstract

Lunar intrusive igneous rocks have not been widely studied in the past; this is related to their rare occurrence in the surface of the Moon, and the difficulty to identify them. Most of the known structures of this type were discovered with telescopic images and were identified as intrusive domes, which are characterized by their oval shape, low slope, and subtle effect in the topography. We analyzed one of these systems with modern datasets and techniques, the Valentine domes, located near the rim of the west Serenitatis basin. We created a geostratigraphic map of the zone, combining geomorphological and spectral classifications. The aspect map turned out to be the most suitable product to search and delimit these structures, it also allowed the identification of a new dome southeast of the principal body, meaning the intrusive system is bigger than previously thought. From the detailed mapping, it was found that the three domes can be classified as laccoliths; and that several secondary structures such as rilles, dykes, and secondary domes record different stages of intrusive activity in the location. A crater counting analysis revealed that the system was active at least until 1.88 Ga ago. Finally, similar intrusive bodies on Earth host ore minerals, which highlights their importance as a target for future exploration.

Plain Language Summary

Igneous rock assemblages other than lunar maria have not been extensively studied, in part due to their limited extent. In this work, we analyzed and made a comprehensive map of the Valentine Domes system near the rim of the Serenitatis basin, a group of igneous structures derived from the cooling and emplacement of magma below the surface. These types of domes are difficult to identify in satellite imagery due to their subtle effect on the topography, but modern datasets allowed us to discover a new dome, on top of studying the ones already known. The detailed mapping allowed the identification of several secondary structures around the main domes, which proved the igneous system was more complex and bigger than previously thought. Our analyses suggest that the igneous system was active at least until 1.8 Ga ago. Back on Earth, intrusive domes are an important source of minerals, so these locations on the Moon might be worth exploring in the future.

1 Introduction

The lunar geological activity has been largely dominated by igneous and impact-related processes (e.g. Schultz and Spudis, 1983). Large impacts are responsible for the formation of the major basins, as well as the accumulation of large amounts of regolith on the surface (e.g. Geiss and Rossi, 2013; Liu et al., 2021). Extrusive igneous processes have also been important since the sustained emission of basaltic lavas has shaped the emblematic lunar “maria” (e.g. Taylor, 1976). Other expressions of extrusive activity can be found around the Moon. Large volcanic complexes exist, like Mons Rümker (Scott and Eggleton, 1973) or Marius Hills (McCauley 1967), but several small-scale landforms dominate the diversity of lunar volcanism. Lunar rilles carved by lava flows are commonly found in the maria (Garfinkle 2020), in some cases associated with pits of high scientific interest (Wanet and Robinson 2014). Less common are pyroclastic deposits, which can be associated with cinder cones or fractures in the surface (Gustafson et al., 2012). Although the influence of extrusive igneous activity on the lunar surface is substantial as seen in the previous examples, that is not the case for intrusive igneous processes.

1.1 Intrusive rocks on the Moon

The absence of widespread intrusive bodies on the lunar surface is related to the mechanisms of intrusive activity itself. The ascension of magmatic bodies that cooled under the surface is controlled by the buoyancy of both the intrusion and the host rock, and the distribution of stress in the crust (Hutton, 1988). In contrast to Earth, on the Moon there is no widespread mechanism like crustal contamination that allows magma coming from the mantle to evolve and surpass the density difference with the lighter upper crust (e.g. Shearer et al., 2006, Wieczorek et al., 2006). This makes the ascension of the magma difficult, so the intrusive bodies tend to cool down and stall in the lower crust (e.g. Cahill et al., 2009). Nevertheless, some fragments of rocks returned during the Apollo missions have been interpreted as intrusive in origin (Papike et al., 1998). Two distinct groups of rocks arose from this analysis, the Mg-suite, characterized by the presence of silicates with high contents of magnesium (Shearer et al., 2015); and the Al-suite, enriched in alkaline elements and with remarkable concentrations of rare elements (Snyder et al., 1995). The named samples were found both as complete fragments or as small aggregates in lunar breccias, and an estimated crystallization depth of 40-50 km was set for them (Shearer et al., 2015).

Considering the already mentioned internal conditions of the Moon, there are only two ways in which these fragments (or any other intrusive body) could have reached the surface. Either by the excavation of the lower crust or by the intrusion of magmatic bodies in regions where the crust was thinned. Both cases could occur after the impact of large meteorites on the lunar surface (**Figure 1**). Numerical simulations suggest that the biggest impacts on the Moon could have excavated material all the way to the lunar mantle (e.g. Miljković et a., 2015). Through this process, rocks of the Mg-suite and Al-suite would reach the surface as ejecta or in the structurally uplifted central peaks of complex craters (Klima et al., 2011, Bretzfelder et al., 2020). Another consequence of the excavation made by large impacts was the thinning and fracturing of the crust, which was followed by the upwelling of magma from the mantle and the subsequent eruption of large quantities of flood basalts that filled the impact craters (Hartmann and Wood, 1971). This secondary magmatism produced effusive lavas and generated small and relatively shallow intrusions like dykes and domes (Head and Wilson, 2016). Due to their genesis, these secondary intrusions have been found mainly in maria. Dykes and their influence can be commonly found in maria, either directly on the surface as linear or sinuous structures, or below grabens and aligned cinder cones, both landforms that result from a dyke that stalled near the surface (Head and Wilson, 2017).

Intrusive domes appear to be less common, since only a handful of them have been identified, mainly by Lena et al. (2013). Individual domes have not been studied in detail before due to their subtle effect on the surface and the difficulty in locating them. These structures are interesting due to their large size and the geologic processes associated with their emplacement on the lunar surface. Besides, more robust data has been obtained since the work done by Lena et al. (2013), so revisiting intrusive domes at higher resolution was important to further study related geologic processes. To address this situation, in this work we made a geostratigraphic analysis of the Valentine Domes region (30.69° N, 10.20° E), which led us to interpret their origin and infer the properties of lunar intrusive domes in a more general way.

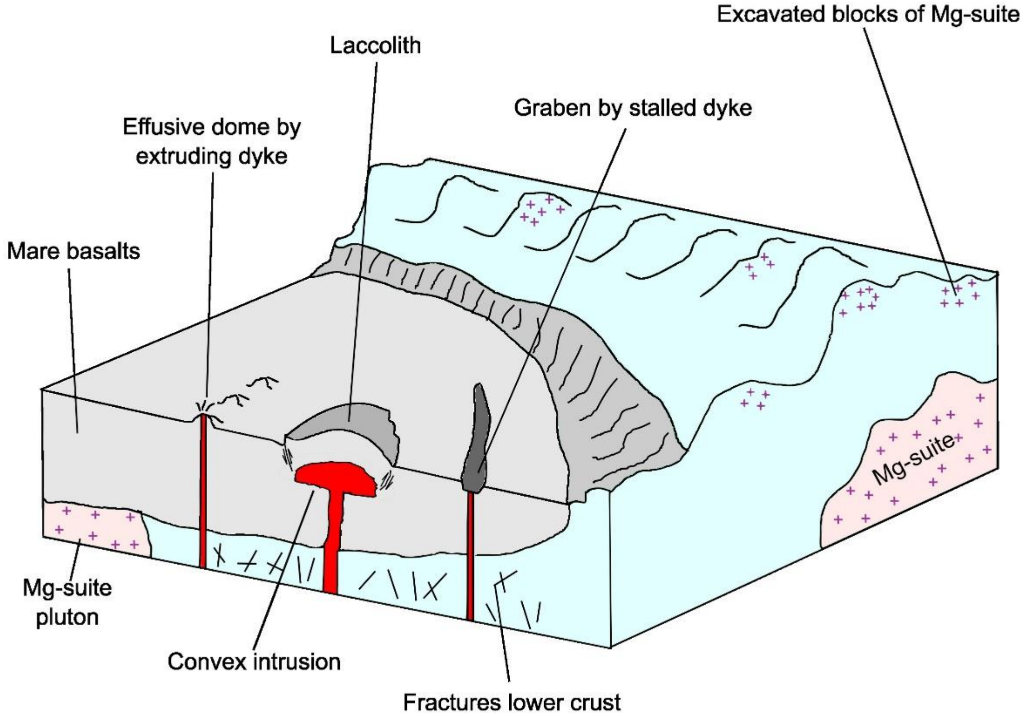

Figure 1: Depiction of the two possible processes that can bring intrusive igneous rock to the surface. The first option is driven by large impacts that excavate intrusive rocks emplaced in the lower crust, and deposit them as ejecta in the rim of the larger lunar basins. In the second case, secondary magmatism is generated in large basins due to the thinning of the crust, the surface expression of these intrusions are laccoliths/intrusive domes (figure not to scale).

1.2 Intrusive domes on the Moon

Lena et al. (2013) defined 16 candidate intrusive domes using telescopic pictures and images from the Wide Angle Camera (WAC) onboard the Lunar Reconnaissance Orbiter (LRO) (Robinson et al., 2010). These structures can be differentiated from effusive domes because they do not have summit or lateral vents, nor lavas flows associated with them. Also, they are typically wider, shorter, and more oval-shaped than other types of domes. These properties make them difficult to locate in optical or spectral images since they do not create an abrupt change in the topography or the composition of the surface. This is especially true in visible images of the maria since the opaque tonalities of the basaltic lavas mask shallow and wide structures like intrusive domes. These domes typically behave as laccoliths, which are convex-shaped uplifts made of pre-existing basaltic lavas, deformed by intruding plutons that stalled near the surface (Schofield et al., 2021). Lena et al. (2013) used the method of Kerr and Pollard (1998) to calculate the depth of the intrusions, obtaining values between 0.5 and 1 km. All the known intrusive domes are located on the maria or transitional zones, suggesting they formed from secondary magmatism after large asteroid impacts.

1.3 Valentine Domes

The Valentine Domes are located in the northwestern region of Mare Serenitatis (30.69 N, 10.20 E), near the rim of the basin (**Figure 2**). The system was originally mapped as volcanic in origin by Hackman (1996). However, it was later described as a possible intrusive system by Lena et al. (2013), consisting of a main dome with a diameter of 30 km (V1), and a secondary dome to the north, with 11 km in diameter (V2). Wöhler and Lena (2009) derived a Digital Elevation Model (DEM) from telescopic images, from which they measured a maximum altitude of 130 m for V1 and 80 m for V2. Lena et al. (2013) highlighted two linear structures for V1, a fault that uplifts the east margin of the dome, and a rille that cuts the structure with an NW-SE trend. According to the global geological map of Fortezzo et al. (2020), both domes are located in Eratosthenian lavas, younger than the Imbrian lavas that dominate the center of the Serenitatis Basin.

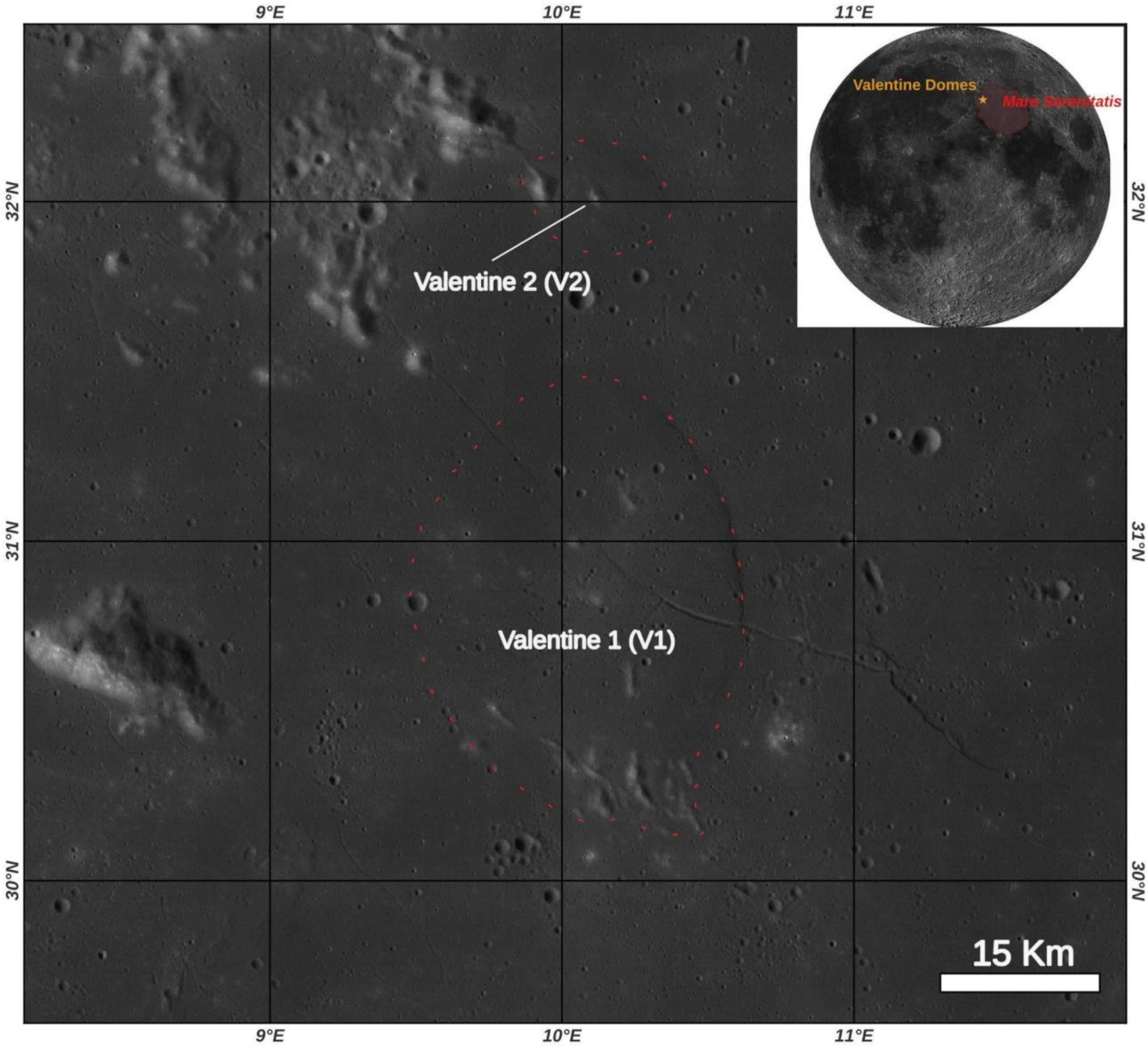

Figure 2: Location of the Valentine domes near the rim of the Mare Serenitatis (30.69° N, 10.20° E). The image is centered in the main dome (V1), it is an oval-shaped structure 30 km in diameter. To the north lies the smaller secondary dome V2, 11 km in diameter.

2 Data

Prior authors used telescopic images since they could achieve low illumination angles, thus generating large shadows and contrasts that allowed them to better identify the shape of the domes. Since then, newer, and more varied datasets have become available, which we used to analyze the domes at high resolution. We utilized two types of panchromatic images, both obtained by the LRO spacecraft. The first one was the global WAC mosaic produced by (Speyerer et al., 2011), with a spatial resolution of 100 m/px. The second type was images from the Narrow Angle Camera (NAC). We obtained 23 images from the Planetary Data System (PDS) (Robinson, 2009), and then created a high-resolution mosaic of the zone with a spatial resolution of 1.5 m/px. We also used two DEMs with different resolutions, the global LRO-Kaguya mosaic produced by Barker et al. (2016), with a resolution of 59 m/px; and a DEM derived from NAC stereo pairs, with a spatial resolution of 3 m/px. To interpret the composition of the surface we generated spectral indexes derived from a hyperspectral cube taken by the Moon Mineralogy Mapper (M^3) onboard Chaandrayan-1 (Green et al., 2011), the cube had a spatial resolution of 110 m/px and contained 85 channels covering the 430 nm-3000 nm spectral range. The cube was downloaded from the PDS (Malaret et al., 2011). Since plagioclase is not easily recognized in M^3 data, we also used the global Christiansen Feature map of Lucey et al. (2021), derived from the Diviner Lunar Radiometer Experiment onboard LRO. Finally, we analyzed the Bouguer gravitational anomalies derived from GRAIL, from the basemaps developed by Goossens et al. (2021). A list of all the products used in this work can be found in **Table S1**.

3 Methods

3.1 Data correction and projection

Data derived from other authors was ready to analyze, but the NAC images and the M^3 cube needed further processing. Both products were treated up to map-projected images using the Integrated Software for Imagers and Spectrometers (ISIS) (Laura et al., 2023) and the Geospatial Data Abstraction Library (GDAL) (Rouault et al., 2023). The processing of NAC images includes the ingestion to ISIS, a radiometric correction, noise correction, map projection, and finally, the generation of a TIF file usable in geospatial software. The processing of M^3 cubes was more convoluted, the importing command of ISIS only accepts the radiance product of M^3, so we modified the associated LBL file of the radiance cube to use the reflectance data (Figuera et al., 2018). After that, the map projection and format transformation were the same. A detailed description of the commands used during these steps can be found in **Text S1**.

2.2 Derived products

We found that a better understanding of the shape of the domes is achieved by studying the DEMs and some products derived from them. The spatial resolution of the LRO-Kaguya DEM is not enough to define small structures, so we created a stereo DEM using the Ames Stereo Pipeline (ASP) (Beyer et al., 2018). We used 5 overlapping NAC images to generate a DEM that covered the entire zone. We created three more products derived from both DEMs using the geospatial software QGIS: a hillshade, a slope map, and an aspect map (**Figure 3**). All of them greatly highlighted the domes and the landforms inside them, but the aspect map was especially useful in delimiting the boundaries of the domes. This is achieved since the aspect records the azimuth direction of the slope, regardless of its magnitude (Florinsky, 2012).

We also derived 28 spectral indexes from the M^3 cube. This process was done using the Python library ***MoonIndex*** (Suarez-Valencia, 2024), which takes as input the map-projected cube and performs the filtering, the removal of the continuum, and then generates a set of spectral indexes useful to survey the mineralogy of the zone. For this case, we applied a convex hull continuum-removal method (Graham, 1972).

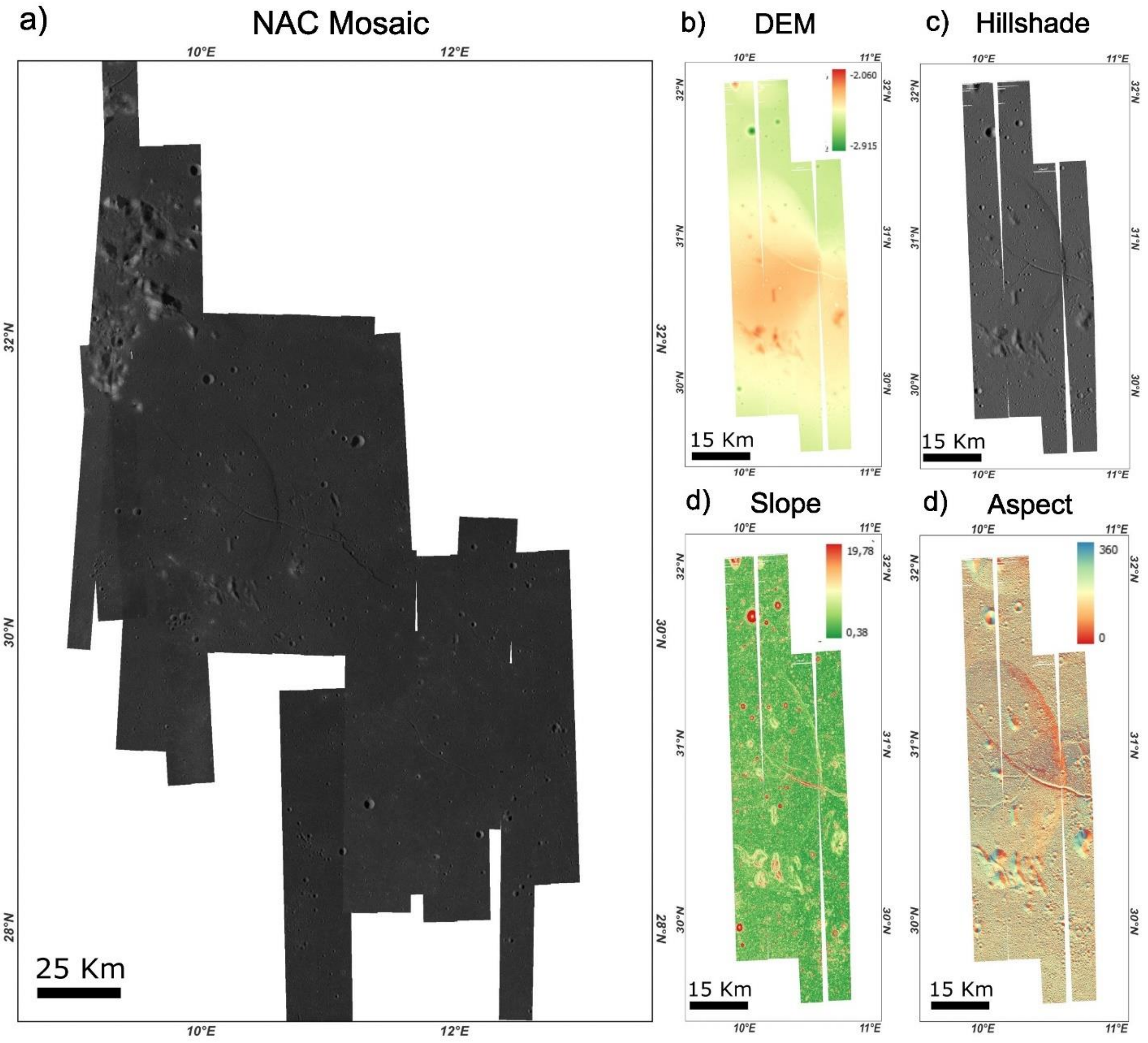

Figure 3: Detailed product used to create the geomorphological map. a) Mosaic of NAC images of the zone, b) DEM of the zone derived from NAC stereo pairs images, c) Hillshade derived from the DEM, d) Slope derived from the DEM, e) Aspect derived from the DEM, the dome is especially clear in this product.

2.3 Mapping techniques

To comprehensively study the Valentine domes, we decided to map them at two scales. On a regional scale, we focused on establishing relationships between the major domes and rilles and how they fit in the geological configuration of the Serenitatis basin rim. At the detailed scale, we mapped just the domes and their surroundings, since several secondary and small landforms lie within them, and are key to understanding the evolution of the intrusive system. We used a hybrid approach to define the units on the map (e.g. Canale et al., 2023; Yingst et al., 2023; Massironi et al., 2021). In this method, the final map is a combination of previously defined geomorphological and spectral maps, defined by a categorized tree of decisions (Yingst et al., 2023). Instead of combining two maps, we decided to first create geomorphological units, which were later refined or modified according to the spectral information (Fassett and Head, 2008; Wright et al., 2024). We followed this approach since in our case the resolution of the panchromatic data is more than ten times higher than the spectral information; also, it would be difficult to create a single spectral map or several maps for each one of the 28 indexes. Finally, we also wanted to incorporate relative ages to the units. For the smallest units this was done by analyzing cross-cutting relationships, and for the larger ones the age was defined using the crater size-frequency counting technique (Neukum et al., 1975, Yue et al., 2022). We also performed a buffer crater-counting analysis to study the relationship between the larger rilles and the domes (Kneissl et al., 2014). The analysis and mapping of the data were done in the geoprocessing software QGIS with the aid of the Mappy plug-in (Penasa, et al., 2023), the crater counting was performed with the CraterTools extension of ArcGIS (Kneissl et al., 2011), and the age determination in the Python version of the software CraterStats (Michael, 2021).

4 Results

Given the properties of intrusive rock complexes, the analysis of the zone at different scales is valuable. We first present the regional mapping, that allowed us to identify large-scale trends of the underlying magmatic complex and other surficial structures not identified by previous authors. We then move to the detailed mapping of the domes, which records the specific properties of the laccoliths and defines the stratigraphic relationships between the different intrusive pulses of the system. The complete maps at both scales can be seen in **Figures S3 and S4**.

4.1 Regional setting

The greatest contrast in the zone occurs between the rim and the mare of the Serenitatis basin. The first one has a bright-tone, scarped topography, and a major abundance of plagioclase, according to the map of Lucey et al. (2021). The mare in turn is dark-toned, has a smooth texture, and is depleted of plagioclase, except for some small structures inside of V1. We also checked the Bouguer gravitational anomaly using the map of Goossens et al. (2021), and although we found a strong positive anomaly from the mare, there is a ring-like structure with a lower anomaly below the intrusive domes (**Figure S1**). The resolution of GRAIL does not allow a detailed analysis of this feature, but this signal might be produced by a buried impact crater.

4.1.1 New dome

As mentioned above, one of the major difficulties of working with intrusive domes is locating them properly. Using the aspect map derived from the Kaguya DEM we were able to identify a new dome (V3) (**Figure 4, Figure 5**). It has a diameter of 43 km on its longer axis, and 33 km on the shorter one, making it the biggest dome of the Valentine system (**Figure 4 a,b**). V3 is oval-shaped and asymmetric, its eastern flank is more pronounced than the western one, but it does not have a steep scarp like V1. The emplacement of this dome had little effect on the surface, as the only noticeable feature in the mare is a narrow linear rille that crosses the dome in an NW-SE direction. It has a gentle slope of 0.43°, compared to the 4.3° of V1, which might be the reason why it was not identified before by Lena et al. (2013). Another interesting feature lies between V1 and V3, the last segment of the long linear rille that dissects V1 is being slightly uplifted in comparison to the rest of the rille. In the aspect map, a linear bump crosses the rille with an NE-SW trend, like the one of the main wrinkle ridges of the zones (**Figure 4a**). Nevertheless, the feature does not resemble a wrinkle ridge, so we interpret it as another incipient uplift generated by an intrusive body. Its shape is irregular, and its borders are diffuse, so we classified it as an incipient dome (**Figure 5**). After discovering these new structures, we evaluated their relationships with the original domes V1 and V2. Using the Kaguya DEM and the aspect map, we identified that a slight bump in the mare contains V1, V3, and the incipient dome (**Figure 4a, c**). The affected region of the mare spans more than 2700 Km^2 and crosses flood basalts of different ages, so it is likely originated from the intrusive system beneath the Valentine region.

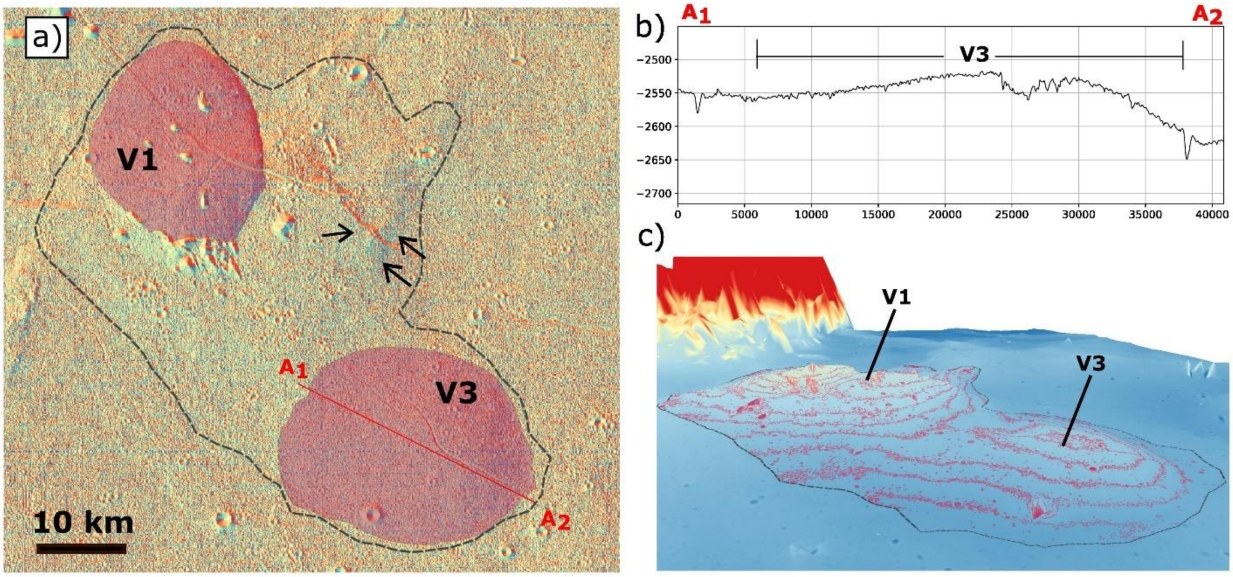

Figure 4: Total area affected by the Valentine intrusive system. a) Location of the newly discovered V3, is the biggest dome of the three, but it has little effect on the surface topography, the arrows point to the incipient dome, b) Profile of V3, the dome is asymmetric, having a steeper slope to the east, c) 3D view of the zone, showcasing the upwelled mare around the two larger domes.

4.1.2 Regional geostratigraphic mapping

The regional geostratigraphic map can be seen in **Figure 5**, the mapping was done with a scale of 1:100.000. Because of its location at the rim of the Serenitatis basin, the zone is largely dominated by highlands and mare units. The igneous units related to the intrusive system are concentrated towards the middle of the zone and will be explained in the detailed mapping.

4.1.2.1 Highlands/rim units

The highlands units make up the rim of the basin, they are characterized by their elevated topography, bright color in optical data, a strong signal of plagioclase, and the relative absence of mafic minerals in the spectral indexes. The most extended unit is Hilly material (***Ihim***), characterized by its abrupt topography and blocky appearance. The main mineral signature is anorthosite, but some escarps show a signal of olivine. This unit probably originated as an ejecta of the impact that created the basin. The other unit in this group is Hummocky material (***Ihum***), which differentiates from ***Ihim*** only by its lower topography and more hummocky texture. According to the map of Fortezzo et al. (2019), both units are Imbrian in age.

An additional highlands unit is Kipuka (***Ik***), these structures are portions of highlands material that were surrounded by mare units, so their optical and compositional properties are the same as other highlands units. Whöler and Lena (2009) classified all the structures inside and around V1 as kipukas, but in this work, we split them between kipukas and secondary intrusive domes.

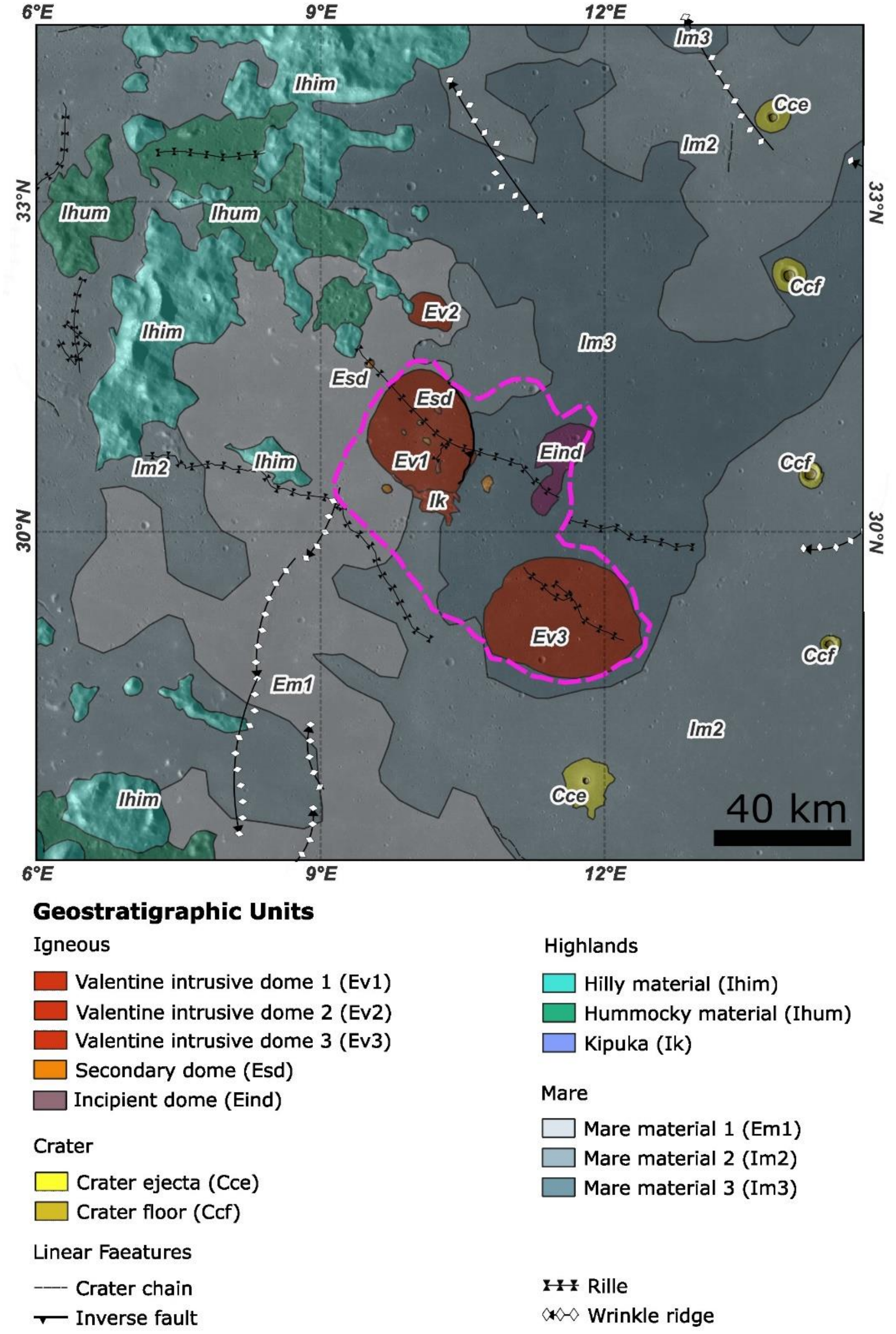

Figure 5: Regional geostratigraphic map of the zone. The total area affected by the main uplift from the intrusive dome is surrounded in pink.

4.1.2.2 Mare units

There are three different pulses of flood lava, which combined are the most extended units in the area. Although the intrusive domes were mapped as units on their own for clarity, it is important to mention that these mare units are the materials on top of the intrusive domes, and thus the actual units at the surface.

Apart from some slight color changes, the three pulses are all dark-toned, flat, and have a smooth texture. Nevertheless, the pulses show variations in composition and age, which was the criteria to divide them. The younger unit, according to Fortezzo et al. (2019) and Hiesinger et al. (2011), is Mare material 1 (***Em1***), it has an age of 2.9 Ga and it is located in the western limit of the basin. Compositionally, it is characterized by its strong signal of mafic minerals. Dome V2 is intruding below this unit, as well as the western part of V1. The unit Mare material 2 (***Im2***) differentiates from the other two due to its high content of spinel. An age of 3.60 Ga was found for this unit using the crater-counting method (**Figure 7**). This pulse spans most of the area on top of V1. Finally, the older flood basalt in the region is Mare material 3 (***Im3***), this unit covers the northeast part of the zone, and it is spectrally similar to ***Em1***. We calculated an age of 3.66 Ga for this unit (**Figure 7**). It covers the entire area of V3.

4.1.2.3 Craters units

Impact craters are common in our zone, all of them are simple craters or crater chains (**Figure 5**). Single craters were mapped as two units, the Crater floor (***Ccf, Ecf***) unit, and the Crater ejecta (***Ece, Ece***) unit, when present. Crater chains were mapped as linear features on the regional scale but as the Crater chain (***Ecc***) unit in the detailed map. The relative age of the craters can be established by the apparent degradation of their rims and ejecta (Agarwal et al., 2019), therefore we classified the ones with clear and bright ejecta as Copernican in age, and the ones without one as Eratosthenian.

4.2 Detailed analysis

The detailed mapping was focused on the intrusive system and was done with a scale of 1:25.000, which allowed us to further discriminate between the intrusive domes and spot differences between them (**Figure 6**). At this scale, structures related to deformation are also more prominent, so several volcano-tectonic units were mapped. Highlands, mare, and crater units are also present in the zone, but there are no changes in the interpretation concerning the regional mapping.

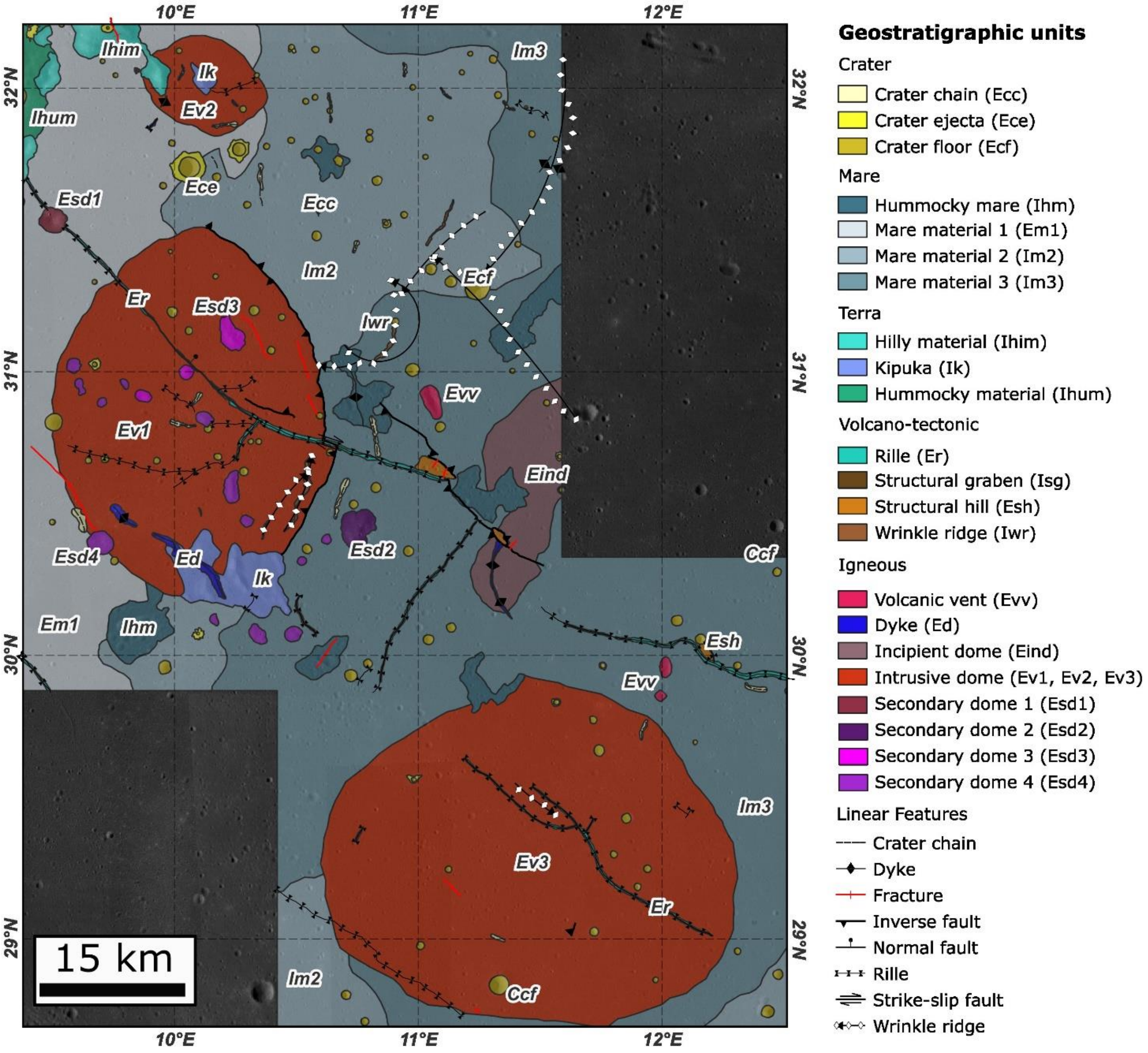

Figure 6: Detailed geostratigraphic map of the zone.

4.2.1 Volcano-tectonic units

We consider volcano-tectonic units those structures that were formed by deformation and fractures triggered by any kind of igneous activity (Azzaro et al., 2012). All the units are located inside the mare, so their composition is equivalent to the one of the lava pulses. The most common volcano-tectonic units are Wrinkle ridges (***Iwr***), they appear as elongated sinuous ridges inside the mare. Their origin has been attributed to the cooling and following thermal contraction of young flood lavas (Watters, 1988), which form small ridges surrounded by thrust faults. Another common structure in the mare are grabens, linear depressions on the surface that can be created by stalled dykes or by extensional stress. The ones created by the later process were mapped as the Structural graben (***Isg***) unit. Last, a couple of Structural hills (***Ish***) were found near the end of the rille that crosses V1, and next to the Incipient dome (***Eind***) unit. These hills are polygonal mesas that are surrounded by steep scarps. The spectral properties of the hills are the same as the flood lavas, so their origin is probably related to the deformation produced by an underlying intrusion, consequent with their closeness to the incipient dome.

4.2.1 Igneous units

Even when the more noticeable igneous structures had an intrusive origin, there were also some extrusive landforms in the zone. A few Volcanic vents (***Evv***) were identified, they are irregular and oval structures, and their border are gentle elevations that surround an inner depression. They are not spectrally different from the mare, and we did not find an anomaly in the band area and asymmetry at the 1 µm band, typical of glass-bearing compositions (Horgan et al., 2014). This means that the vents have not been active in recent geological times. Another extrusive unit was generated by the activity of dykes. Some dykes (***Ed***) were able to reach the surface close to V1 and V2, creating linear ridges that cut other mare units. Their spectral signature is different from the one of the mare units, as the absorption of the mafic minerals is weaker, and the one of the anorthosite is stronger. This type of spectral signature is common to other secondary structures found near the main domes. Dykes also influence the formation of Rilles (***Er***), these are a type of grabens created by the extensional stress generated by a dyke that stalled near the surface (Head and Wilson, 2017). The larger rille on the zone spans more than 50 km and runs from the rim of the basin to the ***Eind*** unit, crossing V1 and other secondary structures. We also found a shorter rille (30 km) on top of V3. The walls of the rilles have a similar spectrum to the mare, but the absorption of mafic minerals is considerably stronger. This is the result of fresher rocks and minerals being exposed by the rille.

Of the three main domes (***Ev2, Ev2, Ev3***), V1 and V2 have several secondary structures on top of them. These structures were originally classified as kipukas by Whöler et al. (2009), but we found that not all of them fit that description. A couple of actual kipukas (***Ik***) were found at the southern limit of V1 and in the middle of V2, they are characterized by their irregular shapes and by having a spectrum like the units from the highlands. The other structures were classified as secondary intrusive domes (***Esd1, Esd2, Esd3, Esd4***), they are remarkably round, are aligned with each other, lie near the main rille, and none of them have volcanic craters on their summits. All of them are inside or near the area of V1, and none around the other domes. Their spectrum is also like the one of the units from the highlands, but they show a higher band depth and a centering at longer wavelengths around the 1 µm band. Both parameters imply a major abundance of mafic minerals compared to the rim units ***Ihum*** and ***Ihim*** (e.g. Adams, 1974; Klima et al., 2011).

4.4 Structural considerations

The rilles, wrinkle ridges, and grabens that were too small to be represented as units were mapped as linear features (**Figure 6**). Regardless of the size, wrinkles ridges have a preferential NE-SW trend, this seems to be a regional pattern since the results were similar in the regional analysis. The zone around V1 is heavily fractured since a network of rilles and faults developed on top of it. Two compressional structures were found. A major thrust fault limits the eastern flank of V1, creating a scarp that reaches 60 m high. The major uplift occurs toward the middle of the dome, where it is cut by the major rille, while to the north and south, the scarp slowly disappears, becoming almost indifferentiable from the mare. The scarp is also displaced horizontally when it meets the major rille, so a strike-slip fault was developed in this location (**Figure S2**). Another major thrust was found to the east of V1, following the end of the major rille, this created a 15 km long scarp and the structural hills of the unit ***Esh***.

Grabens and rilles are the result of extensional stress, and they dominate the zone following two major trends. The main rille cuts the dome in an NW-SE direction, as well as a few other fractures. The middle section of the main rille is not completely developed (thin section of the rille on top of V1 in **Figure 6**), instead an incipient and long normal fault connects the more developed portions of the rille to the north and south. Another major deformation occurs in an almost perpendicular direction, as west to V1, two minor rilles run from the south to the main rille with an NE-SW trend.

4.4 Crater size-frequency distribution

It was difficult to establish the relative age of the domes since the material covering the intrusions corresponds to the flood basalts that originally filled the basin, making a standard crater counting technique not viable since it would only retrieve the age of the lava pulses. Nevertheless, an alternative method known as buffer crater counting can be applied to linear features (Tanaka 1982, Fassett and Head, 2008), and the rilles cutting V1 and V2 are long enough to conduct this analysis. The method consists of counting the craters, or crater ejecta, that intersect the linear feature in question. The total area of the intersecting craters is buffered around the linear feature, and the age is computed in the software CraterStats (Michael 2021; Kneissl et al. 2015). We also applied the usual crater counting technique to the flood lavas on top of both domes. The mapped areas and the resulting ages can be seen in **Figure 7**.

As for the age of the topping flood basalts, the one over V1 has 3.60 Ga, and the one over V3 is 3.66 Ga (**Figure 7b, 7c**). These ages diverge from the ones obtained by Heisinger et al. (2011), which is expected due to the higher scale of our analysis, but the stratigraphic relationships between the units remain the same. The material on top of V3

(***Im3***) is older than the one over V1 (***Im1*** and ***Im2***). Although these ages do not correspond to the intrusion of the domes, they put an upper limit on their formation. The lower limit is given by the ages of the buffered crater counting, which resulted in 1.88 Ga and 2.06 Ga for the two parts of the main rille cutting V1; and 1.81 Ga for the small rille on V3.

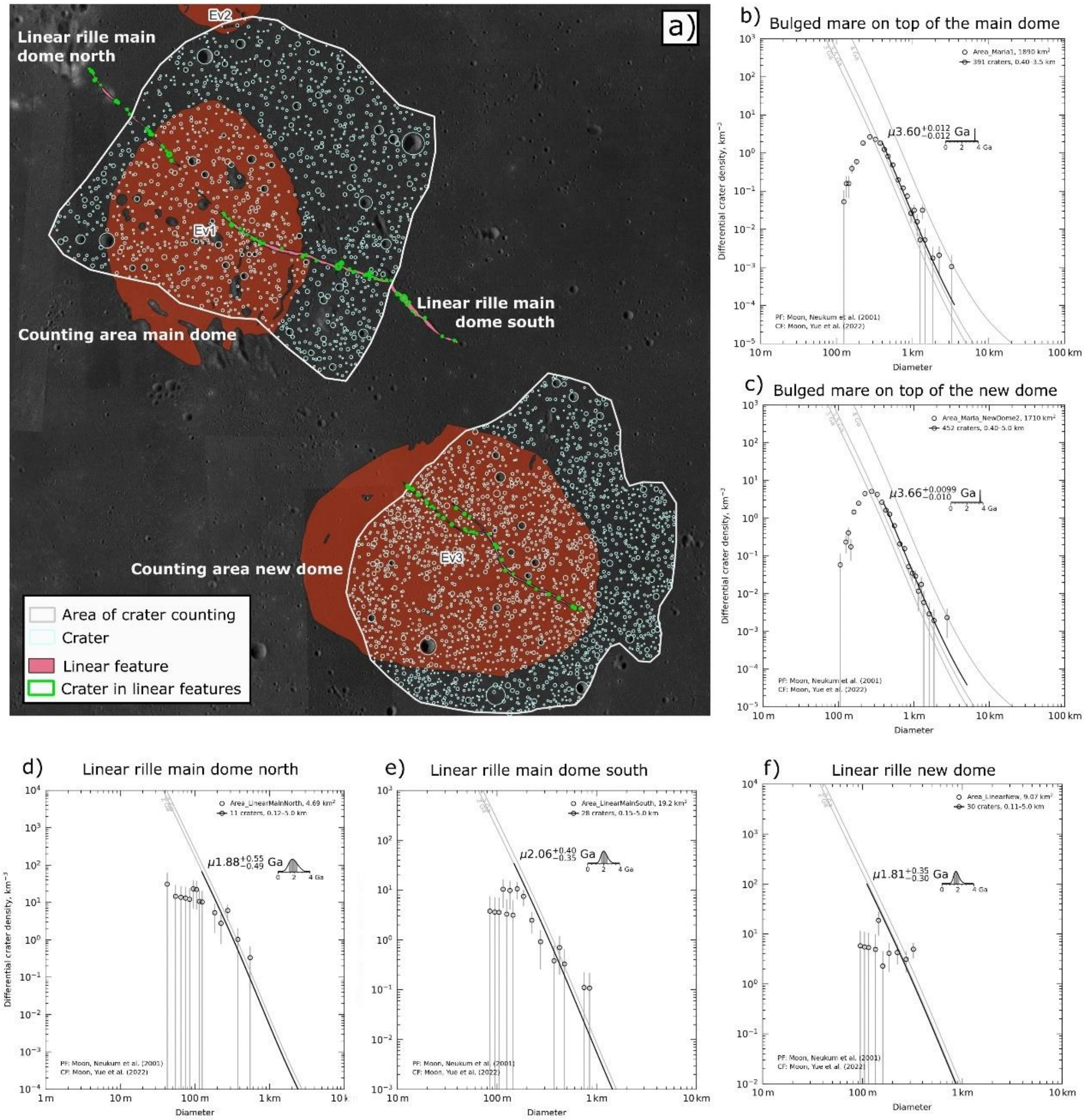

Figure 7: Crater counting analysis. a) The two zones where the normal counting was done are shown in white and the craters counted inside in light blue; the analyzed linear features are pink, and the craters that cut them are green. b) and c) the ages

of the mare on top of V1 and V2, using the normal crater counting method. d), e), f) the age of the linear features using the buffered crater counting method.

5 Discussion

5.1 Kipukas vs Secondary domes

The origin of the secondary structures on top and around V1 has major implications for the geological history of the zone. If they are kipukas, as suggested by Whöler et al. (2009), then intrusive rocks never reach the surface, opposite as if they are secondary domes. The criteria to differentiate them were both geomorphological and spectral. The shape of the structures can be differentiated between irregular and oval-shaped. The irregular ones have a sharp contact with the mare units, and internally they are made of scattered hills. Their texture resembles the one of the rim units, and if they originated as ejecta would be consistent with their lack of orientation. The oval-shaped structures are remarkably round and dome-like, they have diffuse contact with the mare units, and their average height is 100 m, which is lower than the one of the irregular-shaped structures (~250 m). Some of them are aligned in two preferential directions, while the non-aligned ones lie on top or near the main rille. These properties, and their clustering near V1, suggest that the oval-shaped structures originated from an igneous process. The lack of pyroclasts and craters on top of them implies they are not cinder cones, like the ones discovered in other lunar locations (Henderson et al., 2023), so they should be most likely intrusive in origin.

The spectral analysis of these structures helped to further discriminate between them (**Figure 8**). We made an RGB composite where the red channel was the spectral slope at 1 µm, the green channel was the band center at 1 µm, and the blue channel was the band depth at 2 µm (**Figure 8a**). This composition is good to see the difference between the types of secondary structures, the kipukas (***Ik***) and the rim unis (***Ihim)*** have the same orange color, while the secondary intrusive domes appear in various levels of pink. Furthermore, color differences are noticeable between the secondary domes. A dome directly associated with the linear rille appears in bright pink (***Esd1***), the larger dome in the zone has a red-yellow tone (***Esd2***), a set of domes aligned with an NE-SW trend are pale pink (***Esd3***), and the final group is aligned in an NW-SE trend and has a pink-yellow color (***Esd4***).

We also collected the spectral signatures of all the previous features as well as the background mare (***Im2***), this was done after removing the continuum from the spectra (**Figure 8b**). The weaker absorptions are found in the ***Ik*** and ***Ihim*** units, being the result of a minor abundance of mafic minerals, and further suggesting the same genesis for both units. The unit ***Im2*** shows strong absorptions at 1 µm and 2 µm, typical of pyroxene-rich lavas. All the spectrums of the domes lie between those two types of signatures, suggesting intermediate amounts of mafic minerals. Also, the band center of the domes is located at shorter wavelengths than the ones of the ***Im2*** unit, which points to a major abundance of Mg-rich pyroxenes (Klima et al., 2011). The units ***Esd1*** and ***Esd2***, especially the latter, have an intermedium absorption at 1 µm and a strong absorption at 2 µm, this anomaly is probably related to the presence of spinel, which has a strong absorption around 2 µm, enhancing the typical absorption of pyroxenes (Moriarty et al., 2023). The units ***Esd3*** and ***Esd4*** are darker than the other domes near the visible range and at 1.5 µm, which means they have a higher maturity than the other domes, and thus are older (Lucey et al., 2000).

To confirm that our proposed secondary domes are in fact different from the kipukas and the rim units, we conducted a clustering analysis. Since these structures are small at the spatial resolution of M^3, only a few pixels can be sampled for every unit, so we opted for a visual analysis of the spectra. We plotted the band center at 1 µm versus the band center at 2 µm for the zones highlighted in **Figure 8a,** each plot contains the scatter of the rim unit ***Ihim*** versus one of the secondary structures (**Figure 8c, 8d, 8e**). Since the band center is strongly related to the composition (e.g. Adams, 1974), we would expect a strong clustering of the points if the composition of both units was similar. **Figure 8c** plots the distribution of the units ***Ihim*** and ***Esd3***, although some pixels of both units overlap (black), the majority of the points of ***Ihim*** are clustered at shorter band centers (green), and the ones of ***Esd3*** are concentrated at longer centers (blue). This indicates that this set of secondary domes is spectrally different from the rim material, further pointing to a difference in their origin. A similar result was found for ***Ihim*** and ***Esd4*** (**Figure 8d**). On the other hand, the same exercise for the ***Ik*** and ***Ihim*** units returned a contrasting result (**Figure 8e**), in this case, the points for both units are scattered with not clear clusters, so the units cannot be spectrally differentiated. From this analysis, we corroborated that the ***Ik*** unit is indeed compositionally closer to the rim units, and probably genetically unrelated to the other secondary structures.

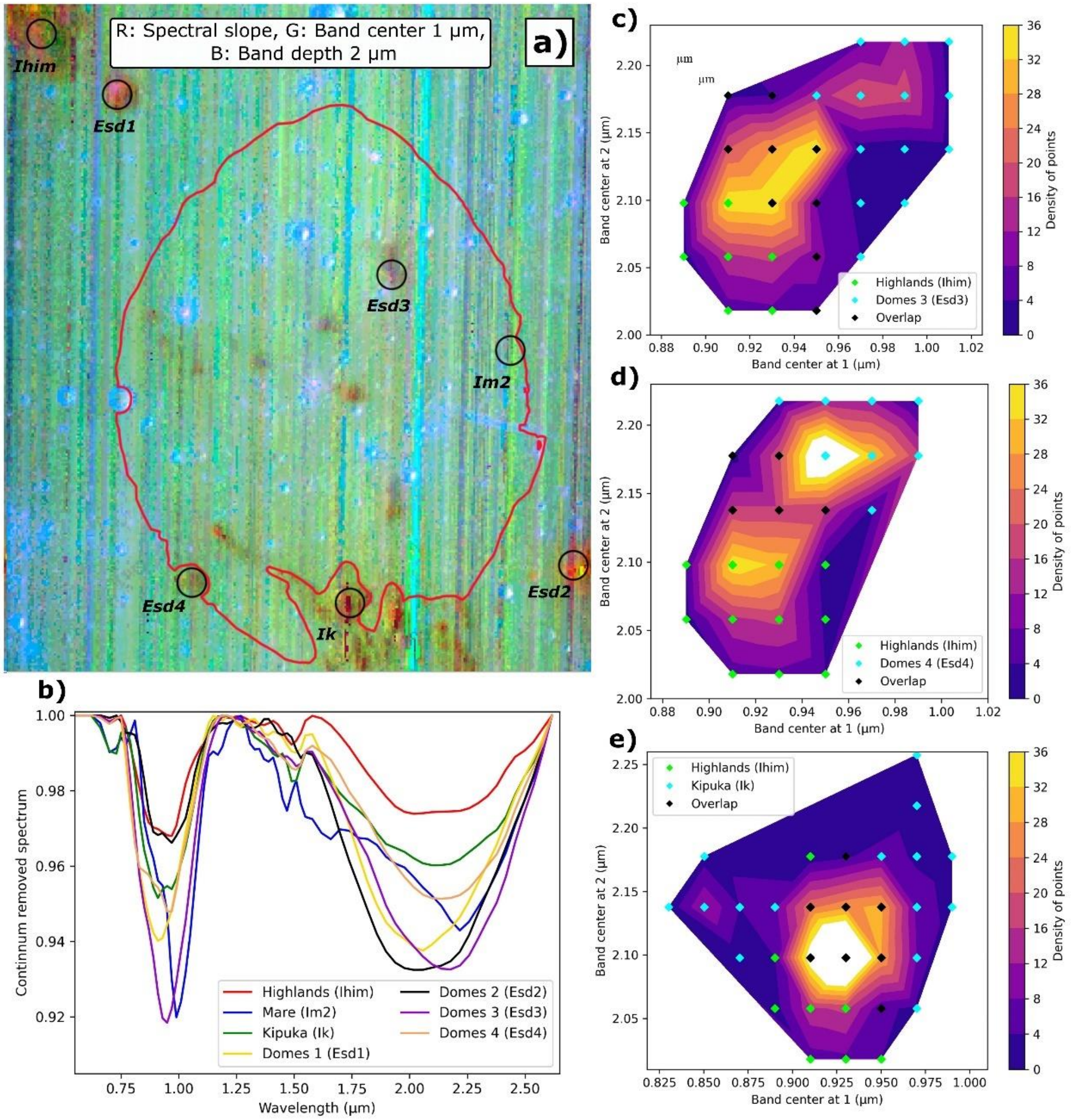

Figure 8: a) RGB composite showing spectral differences between the groups of domes (*Esd1, Esd2, Esd3, Esd4*), kipukas (*Ik*), rim unit (*Ihim*), and mare (*Im2*). b) Plot of the spectra of the different units after the continuum removal, the zones sampled are highlighted by black circles in Figure 8a. The weaker absorptions are found in the *Ihim* and *Ik* units, while the strongest in the *Esd2*, *Esd3* and *Im2* units. c) Plot of the band center at 1 μm vs the band center at 2 μm for the pixels inside the black circles in Figure 8a, the contours in the background accounts for the density of pixels plotted. The plot of the band centers for the *Ihim* and *Esd2* units show two clear clusters (cyan and green dots), even if there is some overlap between units (black dots). d) The plot of the *Ihim* and *Esd4* units has a similar result. e) In the

case of the *Ihim* and *Ik*, there are no clear clusters of points, so they are not mineralogically distinguishable.

5.2 Geologic evolution

The reconstruction of events in the region had to rely on both the results of crater counting and the stratigraphic relationships between units (**Figure 9**). Given the relatively small scale of some units, such as the secondary domes, the crater-counting approach was not sufficient. Furthermore, some of the domes are concentrated in small areas, so it was not possible to establish clear stratigraphic relationships. In those cases, their formation times were constrained by contextual geological information, as well as the local geological setting.

The first recognizable event was the formation of the Serenitatis Basin. Previous authors tried to associate radiometric dating ages obtained from lunar samples to the formation of the basin, Černok et al. (2021) found an age of 4.2 Ga, while Spudis et al. (2011) established a lower limit at 3.8 Ga. Its formation is attributed to the impact of a large meteorite, which created the impact basin, and at the same time excavated the ejecta that made up the rim units ***Ihim*** and ***Ihum***, and the kipukas (***Ik***) trapped inside the basin. Another effect of the impact was the thinning and fracturing of the crust, this weakening subsequently allowed the emplacement of extended flood basalts derived from mantle material and impact melt (e.g. Van Dorn, 1969). In our study area, this is represented by three flows: ***Im3*** was the first to be emplaced around 3.66 Ga, then ***Im2*** around 3.60 Ga, and finally ***Em1***, which was dated at 2.98 Ga by Heisinger et al. (2011) (***Im3*** and ***Im2*** were dated in this work). The formation of wrinkle ridges (***Iwr***) and structural grabens (***Isg***) is related to the thermal accommodation of the flood basalts (Watters, 1988), this happened as soon as the first lava pulse started to cool down and continued until the last pulse reached thermal stability. The pair of volcanic vents found in the region (***Evv***) could have formed as early as the emplacement of the first lava pulse, but they might also be related to the posterior emplacement of the intrusive domes. The latter seems less likely since the vents do not share spectral or structural properties with the intrusive system.

The emplacement of the large domes ***Ev1***, ***Ev2***, and ***Ev3*** is related to the intrusion of a large igneous complex below the area. The location of the intrusive system near the rim of the basin suggests that the upwelling magma took advantage of the large annular faults typically formed at the edges of the lunar impact basins (Collins et al., 2022). The domes have an asymmetric shape, low topography, and sometimes faulted scarps, which are typical properties of laccoliths (Schofield et al., 2021). However, these structures prove difficult to date since a crater counting exercise on them only retrieves the age of the topping flood lavas. We know for sure that they formed after all the lava pulses extruded (after 2.98 Ga), since the three mare units are uplifted by at least one dome. We also know that they predate, or at least formed synchronously with the large rilles (***Er***) on top of V1 and V2. These linear features are the result of intruding dykes stalled near the surface, which were also fed by the larger intrusive body. The rilles are dated between 1.81 and 2.06 Ga, which would also be the lower limit to the formation of the laccoliths.

At least V1 continued raising after this time, since the main rille is slightly uplifted where it crosses the thrust fault limiting V1 to the east. The secondary domes ***Esd1***, ***Esd2***, ***Esd3***, and ***Esd4*** are small intrusions likely related to intruding dykes. Even if only ***Esd1*** is clearly superimposed to the main rille, the alignment of the other sets of domes points to a similar origin. This means that these later domes formed after 1.88 Ga. We know that the four groups are mineralogically different, meaning that they formed from different sources of magma and probably at different times. Nevertheless, we could not establish stratigraphic relationships between them to further discriminate their temporality. Our mapping suggests that ***Esd1*** and ***Esd2*** are younger, due to their sharp borders and higher reflectance in the visible range.

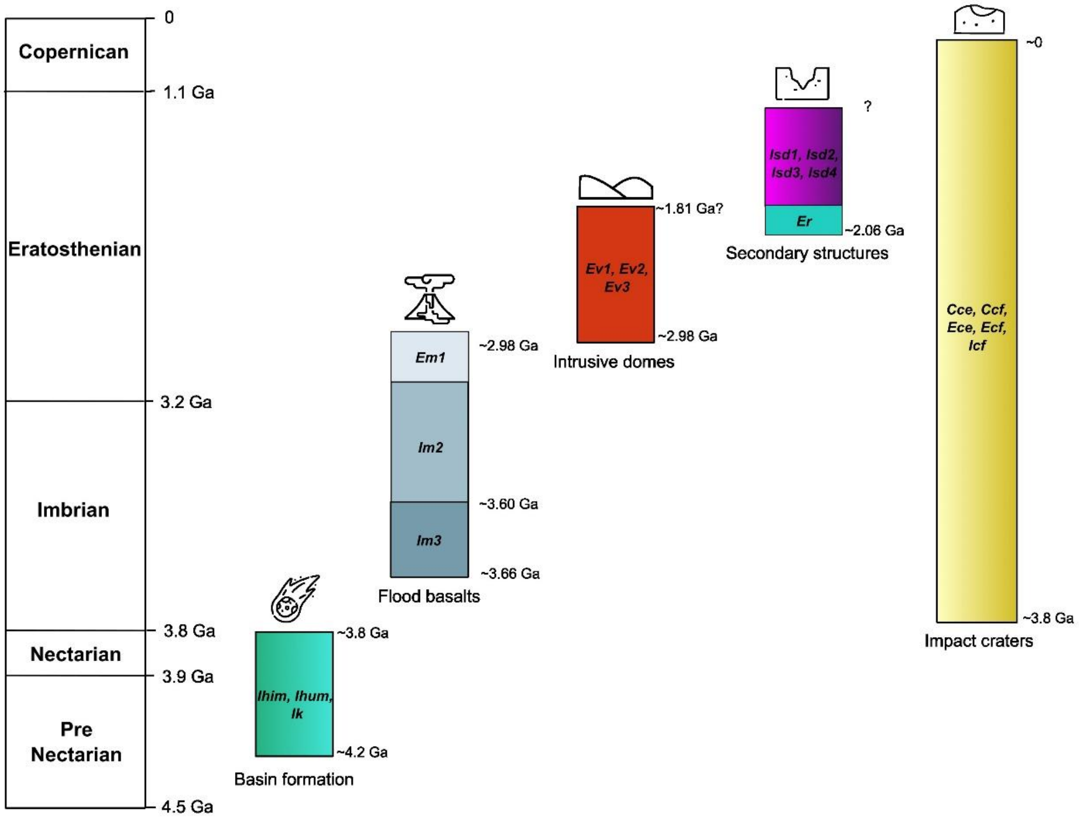

Figure 9: Geological history of the zone. The Serenitatis basin and its rim were formed by a meteorite impact, this created the rim units and kipukas, and triggered the emplacement of flood lavas. The main domes intruded after the last lava pulse and the formation of the main rilles, and was followed by the formation of dykes, secondary domes and smaller rilles. Finally, meteorites impacts have occurred throughout the history of the zone.

5.3 Potential reservoirs

On Earth, intrusive bodies are important deposits of mineral resources. Some of them are hosted in the intrusive itself, like the Stillwater complex in the United States

(Page, 1977), and others are generated by derived processes, like the skarns in the Yeshan deposit in China, formed by contact metamorphism (Zhao et al., 2022). There is a potential for the Valentine domes and other secondary domes to host minerals of interest for the upcoming lunar exploration. However, there are some differences between the intrusions of the Earth and the ones on the Moon. The lunar crust and mantle are at least moderately depleted of water (Hauri et al., 2015), this difficult the mobilization of minerals in a zone with potential contact metamorphism, which is the main mechanism of mineral concentration in these systems. Furthermore, the dominant composition of the lunar rocks is basaltic, as is the case in the Valentine domes, so deposits related to felsic intrusions would not be common, apart from some specific cases like the Gruithuisen domes (e.g. Braden and Robinson, 2011). Given this context, mineralizations in lunar intrusions would be more similar to the ones where the desired ores are hosted inside the intruding mafic rocks themselves, like the Stillwater complex or the great Zimbabwe dyke (Wilson, 1996). Some valuable materials accumulate in those settings, especially iron, elements of the platinum group, and chromites. The main dome of the Valentine system has an interesting advantage in the thrust fault that defines its eastern flank, intrusive rocks may be outcropping along this structure, facilitating access to potential mineralizations; and most importantly, the fault itself and the network of fractures associated to it can act as a weak zone were mobilized minerals can be hosted. Finally, although the data of M^3 is good enough to analyze the general mineralogy of a region, datasets with more resolution would be necessary to address the real potential of ore minerals in these systems, as well as the recovery of physical samples that could be analyzed in the laboratory.

6 Conclusions

Intrusive domes are probably one of the least studied landforms on the Moon. This is the case because intrusive processes are rare due to their subtle effects on the surface. We found that given their low topography, large extent, and small slope, the aspect map is a key product to identify them. This product clearly shows the direction of the slope, indifferently of its magnitude, thus highlighting the real boundaries of the domes. We believe that there are still plenty of intrusive domes that have been overlooked in remote sensing data, and closer observation of high-resolution DEMs and aspect maps may reveal new domes hidden in plain sight, like V3.

Intrusive domes are medium-sized structures that tend to be clustered, so the use of low-resolution data to study them is challenging. Some datasets like the gravitational anomaly derived from GRAIL are too coarse to retrieve meaningful information, but products with medium resolution like M^3 can be useful. Even if a spectral analysis of an intrusive dome will mainly return information of the topping units, something can be obtained from secondary structures. In the case of the Valentine system, the secondary structures were too small to use the spectral data of M^3 as the primary means of classification. Nevertheless, with a previously generated geomorphological map, it was possible to spot and contextualize clear differences between units using spectral indexes and clustering spectral parameters.

The intrusive system beneath the Valentine dome is bigger than previously known, the newly discovered dome V3 is the largest one on the system, and together with V1, they are part of a bigger uplifted zone. The secondary structures on top of V1 are compositionally different from the rim units, meaning they are also igneous in origin. These structures record the history of an intrusive system that was active for several million years, after 2.98 Ga and at least until 1.88 Ga ago. The number of secondary domes, fault systems, and dyke networks on V1 implies that the intrusion is closer to the surface in this location, and portions of the intruding rocks may even outcrop in the secondary domes and across the large thrust fault bounding the east flank of the V1. Although it is not possible to establish the detailed composition of these intrusive rocks, they might host ore minerals like their counterparts on Earth, making them an interesting location for future exploration.

Acknowledgments

This research was done on the framework of the EXPLORE project, which received funding from the European Union’s 2020 research and innovation program under grant agreement No 101004214. Additionally, we had support from the GMAP project, part of the Europlanet 2024 RI that has received funding from the European Union's Horizon 2020 research and innovation programme under grant agreement No 871149.

Open Research

The raw datasets used in this work can be accessed through the PDS. The ***MoonIndex*** software is available for Python 3.10 and higher in the PyPI repository. The source code, exemplary Jupyter notebooks, definition of functions, and workflows can be accessed via GitHub and Zenodo (Suárez-Valencia, 2024). The processed geospatial dataset, QGIS project, and final maps can also be accessed via Zenodo (Suárez-Valencia and Rossi, 2024).

References

Adams, J. B. (1974). Visible and near-infrared diffuse reflectance spectra of pyroxenes as applied to remote sensing of solid objects in the solar system. Journal of Geophysical Research, 79(32), 4829-4836. https://doi.org/10.1029/JB079i032p04829

Agarwal, N., Haridas, A., Khanna, N., Srivastava, P., & Jain, V. (2019). Study of morphology and degradation of lunar craters using Chandrayaan–1 data. Planetary and Space Science, 167, 42-53. https://doi.org/10.1016/j.pss.2019.01.003

Aileen Yingst, R., Mest, S. C., Brent Garry, W., Williams, D. A., Berman, D. C., & Gregg, T. K. P. (2023). A Geologic Map of Vesta Produced Using a Hybrid Method for Incorporating Spectroscopic and Morphologic Data. The Planetary Science Journal, 4(9), 157. https://doi.org/10.3847/PSJ/acebe9

Azzaro, Raffaele. (2012). The volcano-tectonic map of Etna volcano, 1:100.000 scale: An integrated approach based on a morphotectonic analysis from high-resolution DEM constrained by geologic, active faulting and seismotectonic data. Italian Journal of Geosciences, Vol. 131, n. 1, 153-170. https://doi.org/10.3301/IJG.2011.29

Barker, M. K., Mazarico, E., Neumann, G. A., Zuber, M. T., Haruyama, J., & Smith, D. E. (2016). A new lunar digital elevation model from the Lunar Orbiter Laser Altimeter and SELENE Terrain Camera. Icarus, 273, 346-355. https://doi.org/10.1016/j.icarus.2015.07.039

Beyer, R. A., Alexandrov, O., & McMichael, S. (2018). The Ames Stereo Pipeline: NASA's Open Source Software for Deriving and Processing Terrain Data. Earth and Space Science, 5(9), 537-548. https://doi.org/10.1029/2018EA000409

Braden, S. E., & Robinson, M. S. (2011). Human exploration of the Gruithuisen Domes. En W. B. Garry & J. E. Bleacher, Analogs for Planetary Exploration. Geological Society of America. https://doi.org/10.1130/2011.2483(30)

Bretzfelder, J. M., Klima, R. L., Greenhagen, B. T., Buczkowski, D. L., Petro, N. E., & Day, M. (2020). Identification of Potential Mantle Rocks Around the Lunar Imbrium Basin. Geophysical Research Letters, 47(22). https://doi.org/10.1029/2020GL090334

Cahill, J. T. S., Lucey, P. G., & Wieczorek, M. A. (2009). Compositional variations of the lunar crust: Results from radiative transfer modeling of central peak spectra. Journal of Geophysical Research: Planets, 114(E9), 2008JE003282. https://doi.org/10.1029/2008JE003282

Canale, M., Wright, J., & Rothery, D. A. (2024). A hybrid geological map of Sibelius Crater on Mercury, and its associated ejecta and impact melt deposits. Geological Society, London, Special Publications, 541(1), SP541-2022-2296. https://doi.org/10.1144/SP541-2022-296

Černok, A., White, L. F., Anand, M., Tait, K. T., Darling, J. R., Whitehouse, M., Miljković, K., Lemelin, M., Reddy, S. M., Fougerouse, D., Rickard, W. D. A., Saxey, D. W., & Ghent, R. (2021). Lunar samples record an impact 4.2 billion years ago that may have formed the Serenitatis Basin. Communications Earth & Environment, 2(1), 120. https://doi.org/10.1038/s43247-021-00181-z

Collins, M. S., Byrne, P. K., Klimczak, C., & Mazarico, E. (2023). Thrust Faults Bound an Elevated Mantle Plug Beneath Several Lunar Basins. Journal of Geophysical Research: Planets, 128(1), e2022JE007682. https://doi.org/10.1029/2022JE007682

Fassett, C. I., & Head, J. W. (2008). The timing of martian valley network activity: Constraints from buffered crater counting. Icarus, 195(1), 61-89. https://doi.org/10.1016/j.icarus.2007.12.009

Florinsky, I. V. (2012). Morphometric Variables. En Digital Terrain Analysis in Soil Science and Geology (pp. 7-30). Elsevier. https://doi.org/10.1016/B978-0-12-385036-2.00002-X

Fortezzo, C. M., Spudis, P. D., & Harel, S. L. (2020). Unified Geologic Map of the Moon [Map]. Astrogeology. https://astrogeology.usgs.gov/search/map/Moon/Geology/Unified_Geologic_Map_of_the_Moon_GIS_v2

Garfinkle, R. A. (2020). Observing Lunar Rilles, Rupes, and Vallis. En R. A. Garfinkle, Luna Cognita (pp. 941-954). Springer New York. https://doi.org/10.1007/978-1-4939-1664-1_25

Geiss, J., & Rossi, A. P. (2013). On the chronology of lunar origin and evolution: Implications for Earth, Mars and the Solar System as a whole. The Astronomy and Astrophysics Review, 21(1), 68. https://doi.org/10.1007/s00159-013-0068-1

Goossens, S., Fernández Mora, Á., Heijkoop, E., & Sabaka, T. J. (2021). Patched Local Lunar Gravity Solutions Using GRAIL Data. Earth and Space Science, 8(11), e2021EA001695. https://doi.org/10.1029/2021EA001695

Graham, R. L. (1972). An efficient algorith for determining the convex hull of a finite planar set. Information Processing Letters, 1(4), 132-133. https://doi.org/10.1016/0020-0190(72)90045-2

Gustafson, J. O., Bell, J. F., Gaddis, L. R., Hawke, B. R., & Giguere, T. A. (2012). Characterization of previously unidentified lunar pyroclastic deposits using Lunar Reconnaissance Orbiter Camera data. Journal of Geophysical Research: Planets, 117(E12), 2011JE003893. https://doi.org/10.1029/2011JE003893

Hackman, R. J. (1966). Geologic map of the Montes Apenninus region on the Moon [Map]. USGS.

Hartmann, W. K., & Wood, C. A. (1971). Moon: Origin and evolution of multi-ring basins. The Moon, 3(1), 3-78. https://doi.org/10.1007/BF00620390

Hauri, E. H., Saal, A. E., Rutherford, M. J., & Van Orman, J. A. (2015). Water in the Moon’s interior: Truth and consequences. Earth and Planetary Science Letters, 409, 252-264. https://doi.org/10.1016/j.epsl.2014.10.053

Head, J. W., & Wilson, L. (2017). Generation, ascent and eruption of magma on the Moon: New insights into source depths, magma supply, intrusions and effusive/explosive eruptions (Part 2: Predicted emplacement processes and observations). Icarus, 283, 176-223. https://doi.org/10.1016/j.icarus.2016.05.031

Henderson, M. J. B., Horgan, B. H. N., Lawrence, S. J., Stopar, J. D., & Gaddis, L. R. (2023). Mineralogy of explosive and effusive volcanic edifices in the Marius Hills Volcanic Complex. Icarus, 404, 115628. https://doi.org/10.1016/j.icarus.2023.115628

Hiesinger, H., Head, J. W., Wolf, U., Jaumann, R., & Neukum, G. (2011). Ages and stratigraphy of lunar mare basalts: A synthesis. En W. A. Ambrose & D. A. Williams, Recent Advances and Current Research Issues in Lunar Stratigraphy. Geological Society of America. https://doi.org/10.1130/2011.2477(01)

Horgan, B. H. N., Cloutis, E. A., Mann, P., & Bell, J. F. (2014). Near-infrared spectra of ferrous mineral mixtures and methods for their identification in planetary surface spectra. Icarus, 234, 132-154. https://doi.org/10.1016/j.icarus.2014.02.031

Hutton, D. H. W. (1988). Granite emplacement mechanisms and tectonic controls: Inferences from deformation studies. Earth and Environmental Science Transactions of the Royal Society of Edinburgh, 79(2-3), 245-255. https://doi.org/10.1017/S0263593300014255

Kerr, A. D., & Pollard, D. D. (1998). Toward more realistic formulations for the analysis of laccoliths. Journal of Structural Geology, 20(12), 1783-1793. https://doi.org/10.1016/S0191-8141(98)00071-6

Klima, R. L., Pieters, C. M., Boardman, J. W., Green, R. O., Head, J. W., Isaacson, P. J., Mustard, J. F., Nettles, J. W., Petro, N. E., Staid, M. I., Sunshine, J. M., Taylor, L. A., & Tompkins, S. (2011). New insights into lunar petrology: Distribution and composition of prominent low-Ca pyroxene exposures as observed by the Moon Mineralogy Mapper (M 3). Journal of Geophysical Research, 116, E00G06. https://doi.org/10.1029/2010JE003719

Kneissl, T., Michael, G. G., Platz, T., & Walter, S. H. G. (2015). Age determination of linear surface features using the Buffered Crater Counting approach – Case studies of the Sirenum and Fortuna Fossae graben systems on Mars. Icarus, 250, 384-394. https://doi.org/10.1016/j.icarus.2014.12.008

Kneissl, T., Van Gasselt, S., & Neukum, G. (2011). Map-projection-independent crater size-frequency determination in GIS environments—New software tool for ArcGIS. Planetary and Space Science, 59(11-12), 1243-1254. https://doi.org/10.1016/j.pss.2010.03.015

Laura, J., Acosta, A., Addair, T., Adoram-Kershner, L., Alexander, J., Alexandrov, O., Alley, S., Anderson, D., Anderson, J., Anderson, J., Annex, A., Archinal, B., Austin, C., Backer, J., Barrett, J., Bauck, K., Bauers, J., Becker, K., Becker, T., … Young, A. (2023). Integrated Software for Imagers and Spectrometers (7.2.0_RC1) [Software]. Zenodo. https://doi.org/10.5281/ZENODO.2563341

Lena, R., Wöhler, C., Phillips, J., & Chiocchetta, M. T. (2013). Lunar Domes. Springer Milan. https://doi.org/10.1007/978-88-470-2637-7

LRO MOON LROC 2 EDR V1.0. (2009). [dataset]. NASA Planetary Data System. https://doi.org/10.17189/1520250

Liu, T., Michael, G., Zuschneid, W., Wünnemann, K., & Oberst, J. (2021). Lunar megaregolith mixing by impacts: Evaluation of the non-mare component of mare soils. Icarus, 358, 114206. https://doi.org/10.1016/j.icarus.2020.114206

Lucey, P. G., Blewett, D. T., Taylor, G. J., & Hawke, B. R. (2000). Imaging of lunar surface maturity. Journal of Geophysical Research: Planets, 105(E8), 20377-20386. https://doi.org/10.1029/1999JE001110

Lucey, P. G., Greenhagen, B., Donaldson Hanna, K., Bowles, N., Flom, A., & Paige, D. A. (2021). Christiansen Feature Map From the Lunar Reconnaissance Orbiter Diviner Lunar Radiometer Experiment: Improved Corrections and Derived Mineralogy. Journal of Geophysical Research: Planets, 126(6), e2020JE006777. https://doi.org/10.1029/2020JE006777

Marco Figuera, R., Pham Huu, B., Rossi, A. P., Minin, M., Flahaut, J., & Halder, A. (2018). Online characterization of planetary surfaces: PlanetServer, an open-source analysis and visualization tool. Planetary and Space Science, 150, 141-156. https://doi.org/10.1016/j.pss.2017.09.007

Massironi, M., Rossi, A. P., Wright, J., Zambon, F., Poehler, C., Giacomini, L., Carli, C., Ferrari, S., Semenzato, A., Luzzi, E., Pozzobon, R., Tognon, G., Rothery, D. A., Van Der Bogert, C., Galluzi, V., & Altieri, F. (2021). From morpho-stratigraphic to geo(spectro)-stratigraphic units: The PLANMAP contribution. Planetary Geologic Mappers 2021.

McCauley, J. F. (1967). Geologic map of the Hevelius region of the moon. U.S. Geological Survey Report, 491.

Michael, G. G. (2021). CraterStats (2.0) [Python]. GitHub. https://github.com/ggmichael/craterstats#BSD-3-Clause-1-ov-file

Miljković, K., Wieczorek, M. A., Collins, G. S., Solomon, S. C., Smith, D. E., & Zuber, M. T. (2015). Excavation of the lunar mantle by basin-forming impact events on the Moon. Earth and Planetary Science Letters, 409, 243-251. https://doi.org/10.1016/j.epsl.2014.10.041

Moriarty, D. P., Simon, S. B., Shearer, C. K., Haggerty, S. E., Petro, N., & Li, S. (2023). Orbital Characterization of the Composition and Distribution of Spinels Across the Crisium Region: Insight From Luna 20 Samples. Journal of Geophysical Research: Planets, 128(5), e2022JE007482. https://doi.org/10.1029/2022JE007482

Neukum, G., Koenig, B., Fechtig, H., & Storzer, D. (1975). Cratering in the earth-moon system: Consequences for age determination by crater counting. Lunar and Planetary Science Conference Proceedings, 3, 2597-2620.

Page, N. J. (1977). Stillwater Complex, Montana: ROck Succesion, Metamoprhisn and Structure of the Complex and Adjacent Rocks (Professional Paper) [Professional Paper].

Papike, J. J., Ryder, G., & Shearer, C. K. (1998). Lunar samples. Reviews in Mineralogy and Geochemistry, 36(1), 5-01.

Penasa, L., & Brandt, C. H. (2021). europlanet-gmap/mappy: Latest (latest) [Software]. Zenodo. https://doi.org/10.5281/ZENODO.5233646

Robinson, M. S., Brylow, S. M., Tschimmel, M., Humm, D., Lawrence, S. J., Thomas, P. C., Denevi, B. W., Bowman-Cisneros, E., Zerr, J., Ravine, M. A., Caplinger, M. A., Ghaemi, F. T., Schaffner, J. A., Malin, M. C., Mahanti, P., Bartels, A., Anderson, J., Tran, T. N., Eliason, E. M., … Hiesinger, H. (2010). Lunar Reconnaissance Orbiter Camera (LROC) Instrument Overview. Space Science Reviews, 150(1-4), 81-124. https://doi.org/10.1007/s11214-010-9634-2

Rouault, E., Warmerdam, F., Schwehr, K., Kiselev, A., Butler, H., Łoskot, M., Szekeres, T., Tourigny, E., Landa, M., Miara, I., Elliston, B., Chaitanya, K., Plesea, L., Morissette, D., Jolma, A., & Dawson, N. (2023). GDAL (v3.7.1) [Software]. Zenodo. https://doi.org/10.5281/ZENODO.5884351

Schofield, N., Stevenson, C., Mark, N., & Holford, S. (2021). Igneous Intrusions: Sills, Dykes and Plutons. En Encyclopedia of Geology (pp. 313-329). Elsevier. https://doi.org/10.1016/B978-0-08-102908-4.00112-0

Schultz, P. H., & Spudis, P. D. (1983). Beginning and end of lunar mare volcanism. Nature, 302(5905), 233-236. https://doi.org/10.1038/302233a0

Scott, D. H., & Eggleton, R. E. (1973). Geologic map of the Rumker Quadrangle of the Moon. https://doi.org/10.3133/i805

Shearer, C. K. (2006). Thermal and Magmatic Evolution of the Moon. Reviews in Mineralogy and Geochemistry, 60(1), 365-518. https://doi.org/10.2138/rmg.2006.60.4

Shearer, C. K., Elardo, S. M., Petro, N. E., Borg, L. E., & McCubbin, F. M. (2015). Origin of the lunar highlands Mg-suite: An integrated petrology, geochemistry, chronology, and remote sensing perspective. American Mineralogist, 100(1), 294-325. https://doi.org/10.2138/am-2015-4817

Snyder, G. A., Taylor, L. A., & Halliday, A. N. (1995). Chronology and petrogenesis of the lunar highlands alkali suite: Cumulates from KREEP basalt crystallization. Geochimica et Cosmochimica Acta, 59(6), 1185-1203. https://doi.org/10.1016/0016-7037(95)00034-W

Speyerer, E. J., Robinson, M. S., & Denevi, B. W. (2011). LUNAR RECONNAISSANCE ORBITER CAMERA GLOBAL MORPHOLOGICAL MAP OF THE MOON. 42nd Lunar and Planetary Science Conference.

Spudis, P. D., Wilhelms, D. E., & Robinson, M. S. (2011). The Sculptured Hills of the Taurus Highlands: Implications for the relative age of Serenitatis, basin chronologies and the cratering history of the Moon. Journal of Geophysical Research, 116, E00H03. https://doi.org/10.1029/2011JE003903

Suárez-Valencia, J. E. (2024). Javierunal16/MoonIndex: Second version of the MoonIndex Python package (2.0.2) [Software]. Zenodo. https://doi.org/10.5281/zenodo.10820503

Suárez-Valencia, J., & Rossi, A. P. (2024). Supporting material for: Geostratigraphic mapping of the intrusive Valentine Domes on the Moon (1.0) [Data set]. Zenodo. https://doi.org/10.5281/zenodo.10849507

Tanaka, K. L. (1982). A new time-saving crater-count technique, with application to narrow features. En NASA Technical Memo, NASA TM-85127 (pp. 123-125). https://ui.adsabs.harvard.edu/abs/1982pggp.rept..123T

Taylor, S. R. (1976). Geochemical Constraints on the Composition of the Moon. 7, 855.

Van Dorn, W. G. (1969). Lunar Maria: Structure and Evolution. Science, 165(3894), 693-695. https://doi.org/10.1126/science.165.3894.693

Wagner, R. V., & Robinson, M. S. (2014). Distribution, formation mechanisms, and significance of lunar pits. Icarus, 237, 52-60. https://doi.org/10.1016/j.icarus.2014.04.002

Watters, T. R. (1988). Wrinkle ridge assemblages on the terrestrial planets. Journal of Geophysical Research: Solid Earth, 93(B9), 10236-10254. https://doi.org/10.1029/JB093iB09p10236

Wieczorek, M. A. (2006). The Constitution and Structure of the Lunar Interior. Reviews in Mineralogy and Geochemistry, 60(1), 221-364. https://doi.org/10.2138/rmg.2006.60.3

Wilson, A. H. (1996). The Great Dyke of Zimbabwe. En Developments in Petrology (Vol. 15, pp. 365-402). Elsevier. https://doi.org/10.1016/S0167-2894(96)80013-3

Wöhler, C., & Lena, R. (2009). Lunar intrusive domes: Morphometric analysis and laccolith modelling. Icarus, 204(2), 381-398. https://doi.org/10.1016/j.icarus.2009.07.031

Yue, Z., Di, K., Wan, W., Liu, Z., Gou, S., Liu, B., Peng, M., Wang, Y., Jia, M., Liu, J., & Ouyang, Z. (2022). Author Correction: Updated lunar cratering chronology model with the radiometric age of Chang’e-5 samples. Nature Astronomy, 6(4), 514-514. https://doi.org/10.1038/s41550-022-01649-4

Zhao, S., Brzozowski, M. J., Mueller, T., Wang, L., & Li, W. (2022). Skarn classification and element mobility in the Yeshan Iron Deposit, Eastern China: Insight from lithogeochemistry. Ore Geology Reviews, 145, 104909. https://doi.org/10.1016/j.oregeorev.2022.104909

Supporting Information for

Geostratigraphic mapping of the intrusive Valentine Domes on the Moon

Javier Eduardo Suarez-Valencia[1], Angelo Pio Rossi[1]

[1]Constructor University Bremen

Contents of this file

Table S1
Text S1
Figure S1 to S4

Introduction

In this supplementary information we first present a table with all the data used to make the geomorphological maps. Next, we showcase the commands used in ISIS to process the RAW data to create interpretation-ready products. The first two supplementary figures illustrate minor analysis and discussions presented in the main text, while the last two are the full-size maps of the Valentine domes.

Table S1.

Name	Instrument/Mission	Data type
WAC_Mosaic (Speyerer et al., 2011)	WAC, LRO	Image
Bouger_Anomaly (Goossens et al., 2021)	GRAIL	Gravimetry
LRO_Kaguya_DEM (Barket et al., 2016)	Kaguya-LRO	DEM
Global_Plagioclase_Map (Lucey et al., 2021)	DIVINER, LRO	Radar
M3G20090204T233457	M^3, Chandrayaan-1	Hyperspectral
M3G20090205T013151	M^3, Chandrayaan-1	Hyperspectral
M1096429144le	NAC, LRO	Image
M1096429144re	NAC, LRO	Image
M1138844838le	NAC, LRO	Image
M1142369182LE	NAC, LRO	Image
M1142369182RE	NAC, LRO	Image
M1142376293LE	NAC, LRO	Image
M1142376293RE	NAC, LRO	Image
M1142383403LE	NAC, LRO	Image
M1142383403RE	NAC, LRO	Image
M1215373653le	NAC, LRO	Image
M1215373653re	NAC, LRO	Image
M1245960358le	NAC, LRO	Image
M1245960358re	NAC, LRO	Image

M1249458276le	NAC, LRO	Image
M1249458276re	NAC, LRO	Image
M1258875804le	NAC, LRO	Image
M1258875804re	NAC, LRO	Image
M1289445702le	NAC, LRO	Image
M1289445702re	NAC, LRO	Image
M1323551881re	NAC, LRO	Image
M1335299652le	NAC, LRO	Image
M181095207le	NAC, LRO	Image
M181095207re	NAC, LRO	Image

Table listing the data used to perform the mapping.

Text S1.

The processing of planetary data requires the use of the ISIS and GDAL software, which was done using the following commands:

Listing all files to do the batch processing

```
ls *.IMG | sed s/.IMG// > Imputs.lis
```

Transformation from IMG to cubes

```
lronac2isis from=\$1.IMG to=\$1.cub -batchlist=Imputs.lis
```

Actualization of cubes kernels

```
spiceinit from=\$1.cub -batchlist=Imputs.lis
```

Calibrating for I/F

```
lronaccal from=\$1.cub to=\$1_lv1.cub -batchlist=Imputs.lis
```

NAC instrumental correction

```
lronacecho from=\$1_lv1.cub to=\$1_lv1echo.cub -batchlist=Imputs.lis
```

Map projection, a map template need to be previously created

```
cam2map from=\$1_lv1echo.cub map=Equirectangular.map to=\$1_lv2.cub
PIXRES=map -batchlist=Imputs.lis
```

Mosaic

```
noseam from=List2.txt to=Final.cub samples=333 lines=333
```

Translate

```
gdal_translate Final.cub Final.tif
```

After these steps, the data is ready for interpretation in a geoprocessing software.

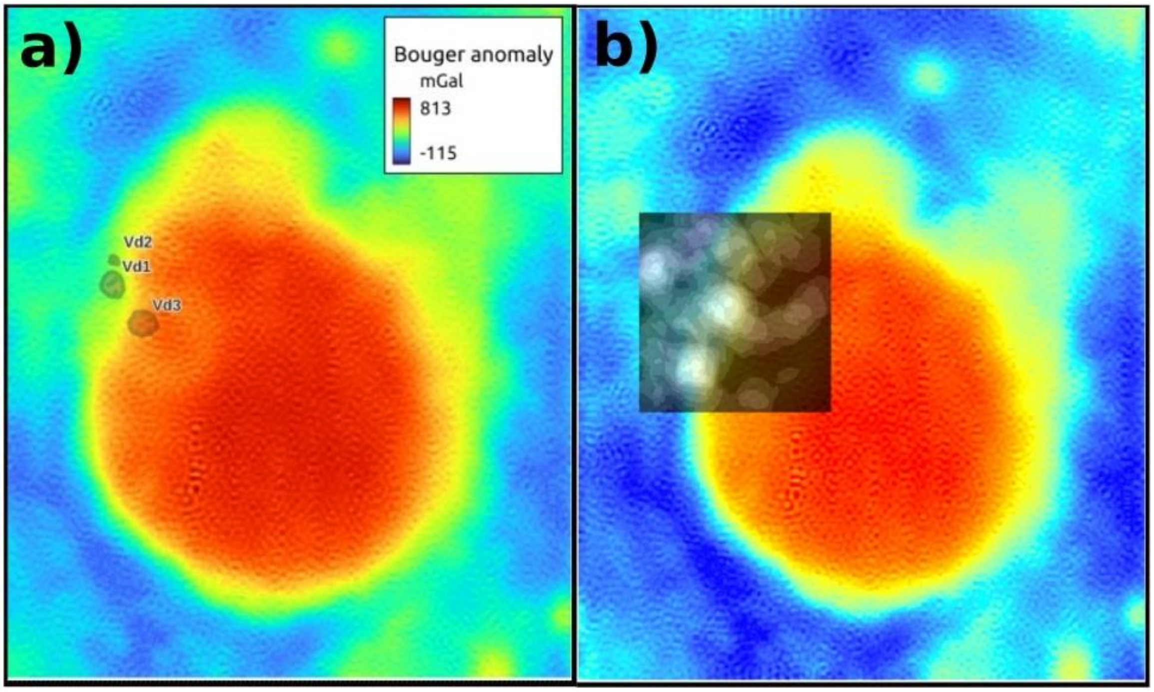

Figure S1. Bouguer anomaly over the valentine domes. a) The mare has a strong positive anomaly, but a ring-shaped structure with a lower anomaly is located beneath the domes. The position of the three domes is shown. b) Line density of the zone, lineaments are concentrated in the rim of the basin and the domes. The underlying structure might be buried crater, which could have weakened the crust more in this location, allowing the emplacement of the intrusive system.

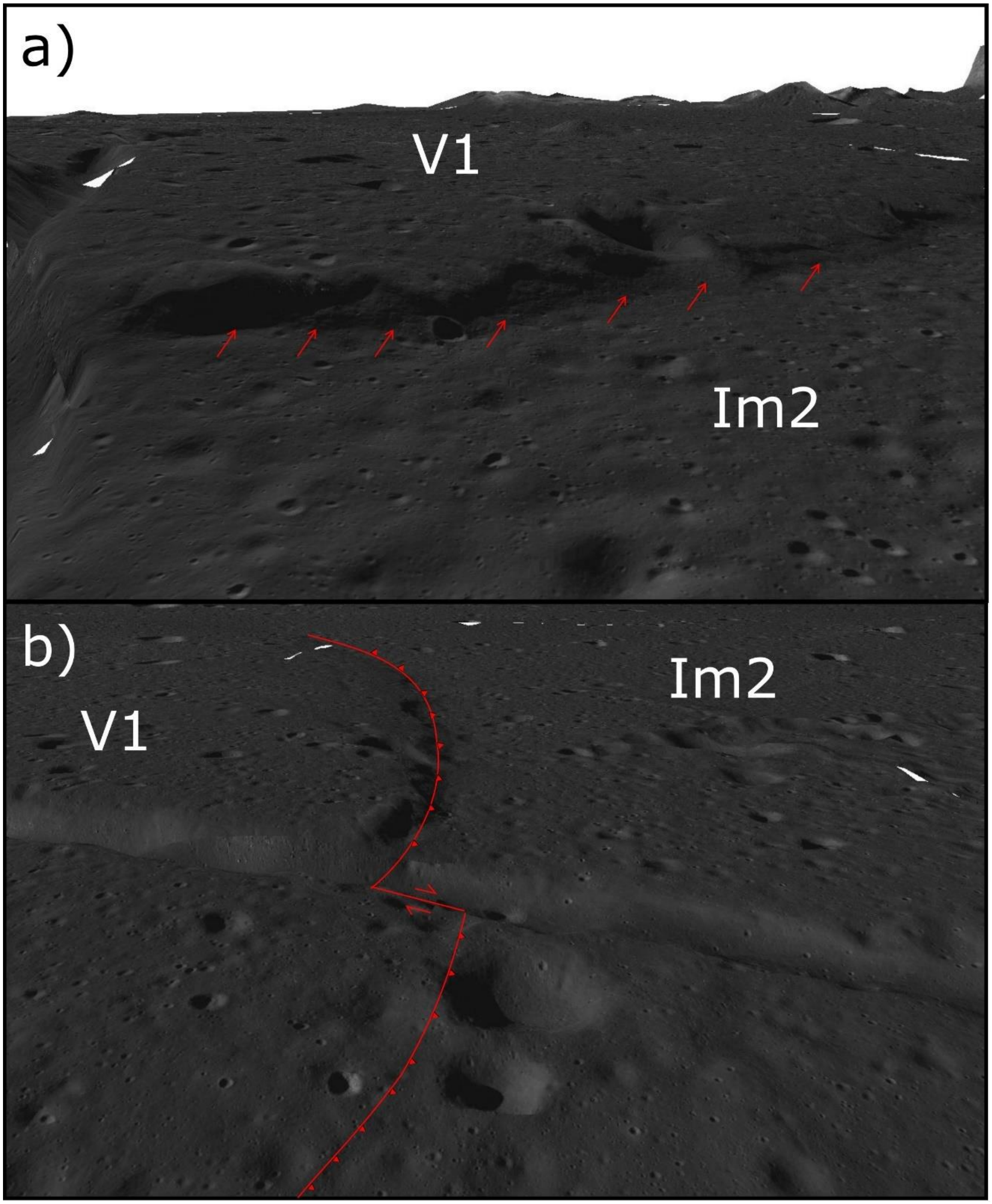

Figure S2. Structural features of V1. a) The east flank of V1 is a scarp up to 60 m high, this section is uplifted by a thrust fault. b) When the mentioned scarp crosses the main linear rille, the feature is translated by a dextral strike-slip fault. South of the rille the scarp is still visible, but it is smaller.

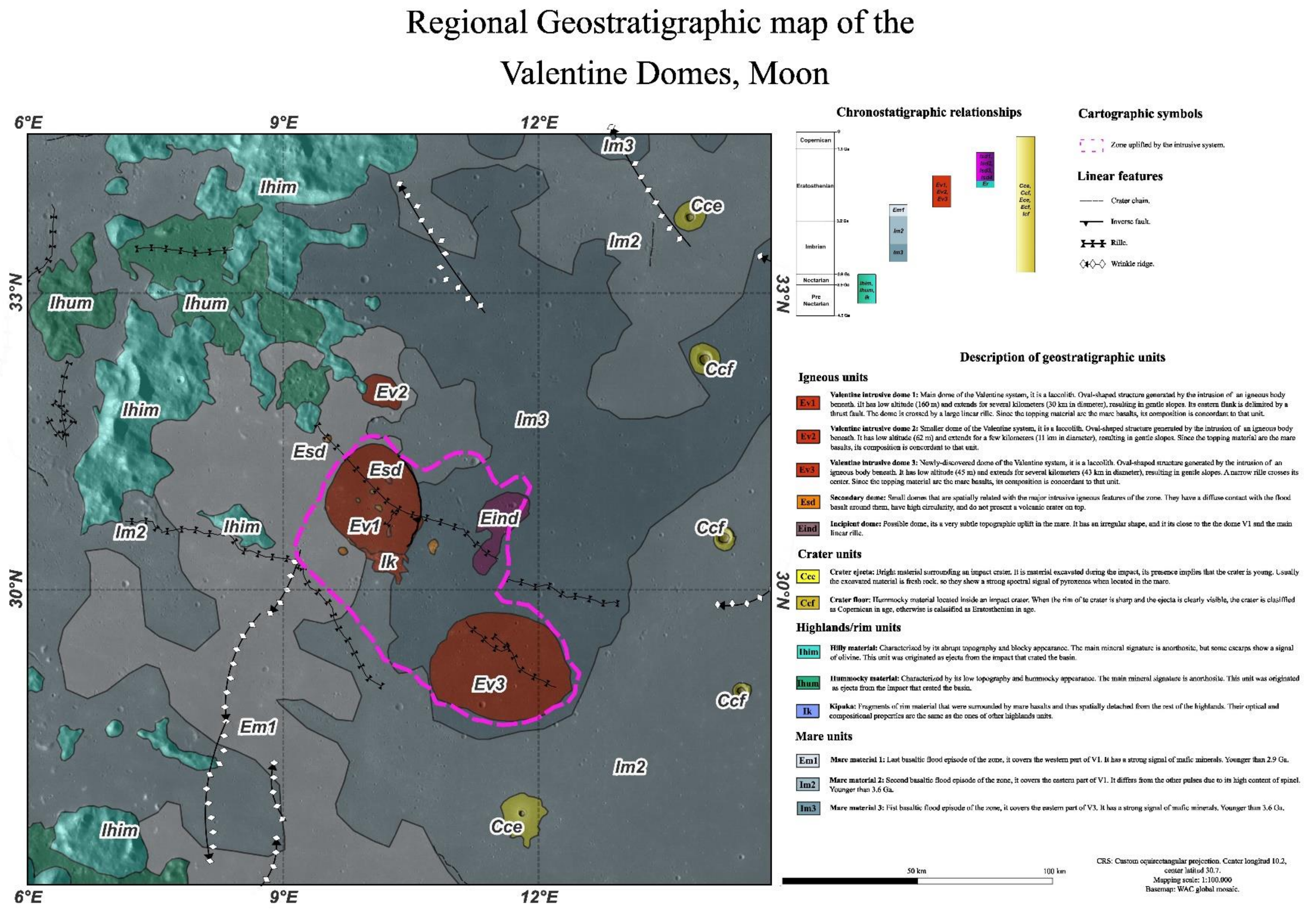

Description of geostratigraphic units

Igneous units

Ev1	**Valentine intrusive dome 1:** Main dome of the Valentine system, it is a laccolith. Oval-shaped structure generated by the intrusion of an igneous body beneath. iIt has low altitude (160 m) and extends for several kilometers (30 km in diameter), resulting in gentle slopes. Its eastern flank is delimited by a thrust fault. The dome is crossed by a large linear rille. Since the topping material are the mare basalts, its composition is concordant to that unit.
Ev2	**Valentine intrusive dome 2:** Smaller dome of the Valentine system, it is a laccolith. Oval-shaped structure generated by the intrusion of an igneous body beneath. It has low altitude (62 m) and extends for a few kilometers (11 km in diameter), resulting in gentle slopes. Since the topping material are the mare basalts, its composition is concordant to that unit.
Ev3	**Valentine intrusive dome 3:** Newly-discovered dome of the Valentine system, it is a laccolith. Oval-shaped structure generated by the intrusion of an igneous body beneath. It has low altitude (45 m) and extends for several kilometers (43 km in diameter), resulting in gentle slopes. A narrow rille crosses its center. Since the topping material are the mare basalts, its composition is concordant to that unit.
Esd	**Secondary dome:** Small domes that are spatially related with the major intrusive igneous features of the zone. They have a diffuse contact with the flood basalt around them, have high circularity, and do not present a volcanic crater on top.
Eind	**Incipient dome:** Possible dome, its a very subtle topographic uplift in the mare. It has an irregular shape, and it its close to the the dome V1 and the main linear rille.

Crater units

Cce	**Crater ejecta:** Bright material surrounding an impact crater. It is material excavated during the impact, its presence implies that the crater is young. Usually the excavated material is fresh rock, so they show a strong spectral signal of pyroxenes when located in the mare.
Ccf	**Crater floor:** Hummocky material located inside an impact crater. When the rim of te crater is sharp and the ejecta is clearly visible, the crater is clasiffied as Copernican in age, otherwise is calssified as Eratosthenian in age.

Highlands/rim units

Ihim	**Hilly material:** Characterized by its abrupt topography and blocky appearance. The main mineral signature is anorthosite, but some escarps show a signal of olivine. This unit was originated as ejecta from the impact that crated the basin.
Ihum	**Hummocky material:** Characterized by its low topography and hummocky appearance. The main mineral signature is anorthosite. This unit was originated as ejecta from the impact that crated the basin.
Ik	**Kipuka:** Fragments of rim material that were surrounded by mare basalts and thus spatially detached from the rest of the highlands. Their optical and compositional properties are the same as the ones of other highlands units.

Mare units

Em1	**Mare material 1:** Last basaltic flood episode of the zone, it covers the western part of V1. It has a strong signal of mafic minerals. Younger than 2.9 Ga.
Im2	**Mare material 2:** Second basaltic flood episode of the zone, it covers the eastern part of V1. It differs from the other pulses due to its high content of spinel. Younger than 3.6 Ga.
Im3	**Mare material 3:** Fist basaltic flood episode of the zone, it covers the eastern part of V3. It has a strong signal of mafic minerals. Younger than 3.6 Ga.

CRS: Custom equirectangular projection. Center longitud 10.2,
center latitud 30.7.
Mapping scale: 1:100.000
Basemap: WAC global mosaic.

Figure S3. Regional geostratigraphic map of the Valentine domes system.

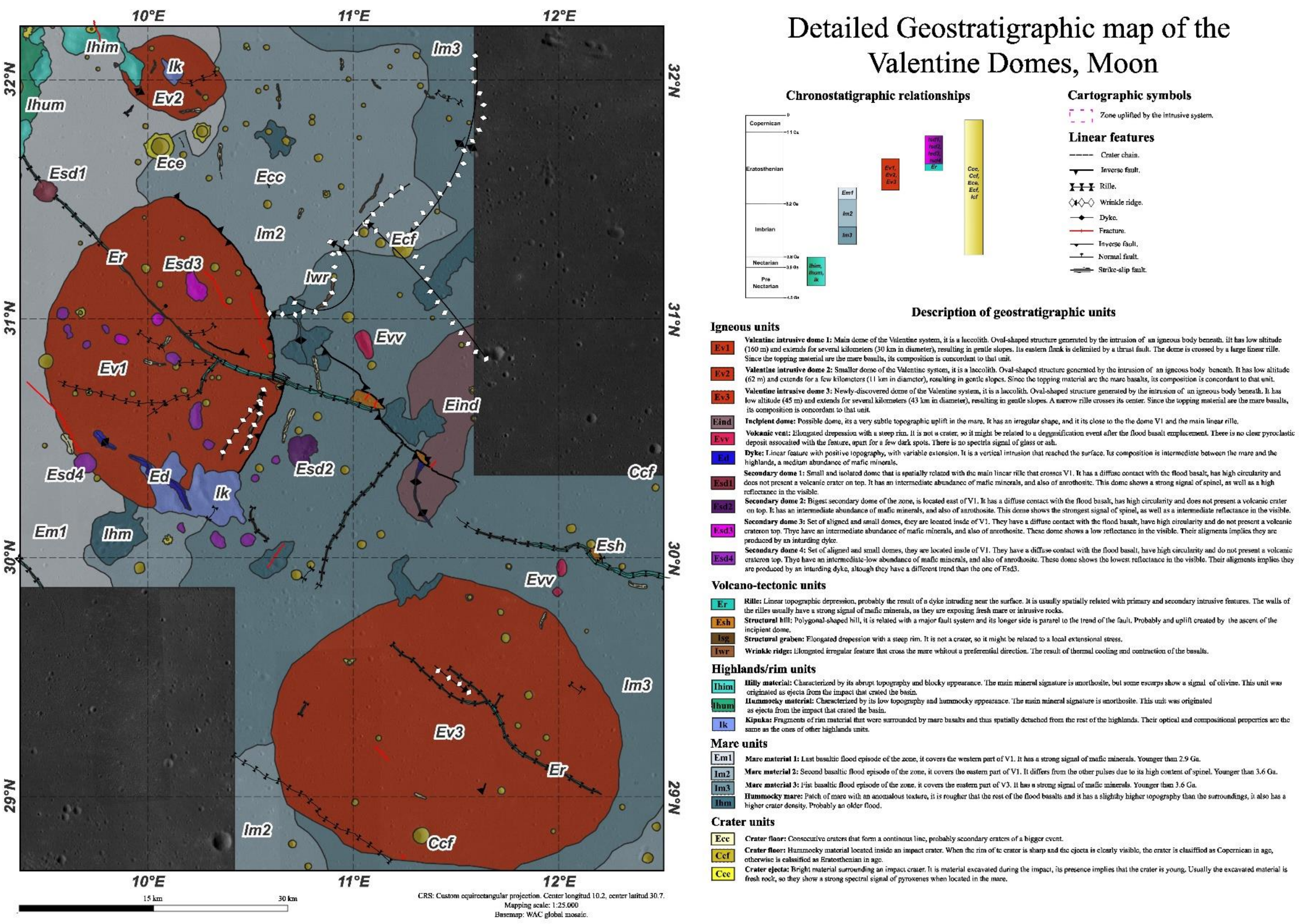

Detailed Geostratigraphic map of the Valentine Domes, Moon

Description of geostratigraphic units

Igneous units

Ev1	**Valentine intrusive dome 1:** Main dome of the Valentine system, it is a laccolith. Oval-shaped structure generated by the intrusion of an igneous body beneath. iIt has low altitude (160 m) and extends for several kilometers (30 km in diameter), resulting in gentle slopes. Its eastern flank is delimited by a thrust fault. The dome is crossed by a large linear rille. Since the topping material are the mare basalts, its composition is concordant to that unit.
Ev2	**Valentine intrusive dome 2:** Smaller dome of the Valentine system, it is a laccolith. Oval-shaped structure generated by the intrusion of an igneous body beneath. It has low altitude (62 m) and extends for a few kilometers (11 km in diameter), resulting in gentle slopes. Since the topping material are the mare basalts, its composition is concordant to that unit.
Ev3	**Valentine intrusive dome 3:** Newly-discovered dome of the Valentine system, it is a laccolith. Oval-shaped structure generated by the intrusion of an igneous body beneath. It has low altitude (45 m) and extends for several kilometers (43 km in diameter), resulting in gentle slopes. A narrow rille crosses its center. Since the topping material are the mare basalts, its composition is concordant to that unit.
Eind	**Incipient dome:** Possible dome, its a very subtle topographic uplift in the mare. It has an irregular shape, and it its close to the the dome V1 and the main linear rille.
Evv	**Volcanic vent:** Elongated drepession with a steep rim. It is not a crater, so it might be related to a deggasification event after the flood basalt emplacement. There is no clear pyroclastic deposit assocaited with the feature, apart for a few dark spots. There is no spectrla signal of glass or ash.
Ed	**Dyke:** Linear feature with positive topography, with variable extension. It is a vertical intrusion that reached the surface. Its composition is intermediate between the mare and the highlands, a medium abundance of mafic minerals.
Esd1	**Secondary dome 1:** Small and isolated dome that is spatially related with the main linear rille that crosses V1. It has a diffuse contact with the flood basalt, has high circularity and does not present a volcanic crater on top. It has an intermediate abundance of mafic minerals, and also of anrothosite. This dome shows a strong signal of spinel, as well as a high reflectance in the visible.
Esd2	**Secondary dome 2:** Bigest secondary dome of the zone, is located east of V1. It has a diffuse contact with the flood basalt, has high circularity and does not present a volcanic crater on top. It has an intermediate abundance of mafic minerals, and also of anrothosite. This dome shows the strongest signal of spinel, as well as a intermediate reflectance in the visible.
Esd3	**Secondary dome 3:** Set of aligned and small domes, they are located insde of V1. They have a diffuse contact with the flood basalt, have high circularity and do not present a volcanic crateron top. Thye have an intermediate abundance of mafic minerals, and also of anrothosite. These dome shows a low reflectance in the visible. Their aligments implies they are produced by an inturding dyke.
Esd4	**Secondary dome 4:** Set of aligned and small domes, they are located insde of V1. They have a diffuse contact with the flood basalt, have high circularity and do not present a volcanic crateron top. Thye have an intermediate-low abundance of mafic minerals, and also of anrothosite. These dome shows the lowest reflectance in the visible. Their aligments implies they are produced by an inturding dyke, altough they have a different trend than the one of Esd3.

Volcano-tectonic units

Er	**Rille:** Linear topographic depression, probably the result of a dyke intruding near the surface. It is usually spatially related with primary and secondary intrusive features. The walls of the rilles usually have a strong signal of mafic minerals, as they are exposing fresh mare or intrusive rocks.
Esh	**Structural hill:** Polygonal-shaped hill, it is related with a major fault system and its longer side is pararel to the trend of the fault. Probably and uplift created by the ascent of the incipient dome.
Isg	**Structural graben:** Elongated drepession with a steep rim. It is not a crater, so it might be related to a local extensional stress.
Iwr	**Wrinkle ridge:** Elongated irregular feature that cross the mare whitout a preferential direction. The result of thermal cooling and contraction of the basalts.

Highlands/rim units

Ihim	**Hilly material:** Characterized by its abrupt topography and blocky appearance. The main mineral signature is anorthosite, but some escarps show a signal of olivine. This unit was originated as ejecta from the impact that crated the basin.
Ihum	**Hummocky material:** Characterized by its low topography and hummocky appearance. The main mineral signature is anorthosite. This unit was originated as ejecta from the impact that crated the basin.
Ik	**Kipuka:** Fragments of rim material that were surrounded by mare basalts and thus spatially detached from the rest of the highlands. Their optical and compositional properties are the same as the ones of other highlands units.

Mare units

Em1	**Mare material 1:** Last basaltic flood episode of the zone, it covers the western part of V1. It has a strong signal of mafic minerals. Younger than 2.9 Ga.
Im2	**Mare material 2:** Second basaltic flood episode of the zone, it covers the eastern part of V1. It differs from the other pulses due to its high content of spinel. Younger than 3.6 Ga.
Im3	**Mare material 3:** Fist basaltic flood episode of the zone. it covers the eastern part of V3. It has a strong signal of mafic minerals. Younger than 3.6 Ga.
Ihm	**Hummocky mare:** Patch of mare with an anomalous texture, it is rougher that the rest of the flood basalts and it has a slighthy higher topography than the surroundings, it also has a higher crater density. Probably an older flood.

Crater units

Ecc	**Crater floor:** Consecutive craters that form a continous line, probably secondary craters of a bigger event.
Ccf	**Crater floor:** Hummocky material located inside an impact crater. When the rim of te crater is sharp and the ejecta is clearly visible, the crater is claiffied as Copernican in age, otherwise is calssified as Eratosthenian in age.
Cce	**Crater ejecta:** Bright material surrounding an impact crater. It is material excavated during the impact, its presence implies that the crater is young. Usually the excavated material is fresh rock, so they show a strong spectral signal of pyroxenes when located in the mare.

CRS: Custom equirectangular projection. Center longitud 10.2, center latitud 30.7.
Mapping scale: 1:25.000
Basemap: WAC global mosaic.

Figure S4. Detailed geostratigraphic map of the Valentine domes system.